



Zhang, T. and Barakos, G. N. (2021) Toward vehicle-level optimization of compound rotorcraft aerodynamics. *AIAA Journal*, (doi: 10.2514/1.J061032).

There may be differences between this version and the published version. You are advised to consult the publisher's version if you wish to cite from it.

<http://eprints.gla.ac.uk/258190/>

Deposited on: 2 November 2021

Enlighten – Research publications by members of the University of Glasgow
<http://eprints.gla.ac.uk>

Towards Vehicle-level Optimisation of Compound Rotorcraft Aerodynamics

T. Zhang*, G. N. Barakos†

CFD Laboratory, School of Engineering, University of Glasgow, G12 8QQ Glasgow, UK.

This paper presents high-fidelity, as well as, simplified CFD modelling approaches within an optimisation framework for compound rotorcraft configurations with rotor/propeller aerodynamic interactions. Simulations of a axial-flight ducted propeller and a rotor/wing test case are first presented to validate the in-house HMB3 solver and to assess the actuator disk/line models for the simplified main rotor modelling. The actuator disk/line models are then used to represent the main rotor for simulations of a generalised rotor/propeller combination. The propeller performance is analysed in detail, and large variations are observed in the single blade loading due to the main rotor wake. A simplified model for the rotor/propeller interaction simulation is also put forward, and an inflow distortion metric is proposed to quantify the aerodynamic interactions. With the help of a Kriging surrogate model and the inflow distortion metric, aerodynamic interferences through the propeller disk are quantitatively visualised with variations in the propeller position, propeller thrust, and main rotor advance ratio. Optimisation of the propeller position under the main rotor for minimised interference with rolling/pitching moment constraints are also attempted using both gradient-based (adjoint) and gradient-free (efficient global optimisation) approaches. The optimisation results are verified using blade resolved simulations, and fluctuations of the propeller single blade loading were effectively reduced due to the optimisation. The work is a first step towards high-fidelity methods for vehicle and configuration optimisation.

Nomenclature

Latin

- a = Speed of Sound, m/s
 b = Wing Span Length, m
 C = Main Rotor Chord, m
 C_p = Pressure Coefficient, $C_p = \frac{P - P_\infty}{0.5\rho a_\infty^2}$

*PhD Student, CFD Laboratory, School of Engineering, Email: t.zhang.4@research.gla.ac.uk

†corresponding author, Professor, SMAIAA, MRaES, CFD Laboratory, School of Engineering, Email: George.Barakos@glasgow.ac.uk

$C_{p_{uns}}$ = Unsteady Pressure Signal, $C_{p_{uns}} = 100 \frac{P - P_{\infty}}{0.5 \rho V_{tip}^2}$
 C_t = Thrust Coefficient, $C_t = \frac{T}{0.5 \rho V_{tip}^2 \pi R^2}$
 C_q = Torque Coefficient, $C_q = \frac{Q}{0.5 \rho V_{tip}^2 \pi R^3}$
 M = Moment, Nm
 I_x = Rotor Inflow Distortion in Axial Direction
 P = Pressure, Pa
 Q = Torque, Nm
 r = Blade Radial Position
 R = Blade Radius, m
 T = Thrust, N
 \mathbf{W} = Conservative Flow Variables

Greek

α_i = Design Variables
 λ = Adjoint Vector
 μ = Advance Ratio, $\mu = \frac{V_{\infty}}{V_{tip}}$
 ν = Kinematic Viscosity, m^2/s
 σ = Actuator Disk Strength
 ψ = Rotor Azimuth, rad
 ρ = Density, kg/m^3

Subscripts and superscripts

∞, inf = Free-stream Value
 x, y, z = x, y, z Directions
 i, j, k = i, j, k Directions
 tip = Blade Tip Value

Acronyms

AD = Actuator Disk
 AL = Actuator Line
 BPF = Blade Passing Frequency
 CFD = Computational Fluid Dynamics

CG	=	Centre of Gravity
eVTOL	=	electric Vertical Take-off Landing
EGO	=	Efficient Global Optimisation
EI	=	Expected Improvement
HMB3	=	Helicopter Multi-Block 3
SST	=	Shear Stress Transport
RANS	=	Reynolds Averaged Navier Stokes
RSD	=	Relative Standard Deviation
URANS	=	Unsteady Reynolds Averaged Navier Stokes

I. Introduction

COMPOUND rotorcraft feature a combination of multiple sources of lift and propulsion from rotary wing systems and lifting surfaces [1]. Through compounding, conventional helicopters can break their inherent speed limitations while maintaining the hover efficiency. The compound rotorcraft are hence a promising choice to bridge the gap between traditional helicopters and fixed-wing aircraft, and fill the mission gap between airplanes and conventional low-speed helicopters[2].

Several design attempts and experimental prototypes can be noted throughout the history of aviation, such as the McDonnell XV-1, Fairey Rotodyne and Kamov Ka-22 in the 1950s, and the Sikorsky S-97 Raider and Airbus X³ in recent decades. More electrical Vertical Takeoff/Landing (eVTOL) concepts, often with multiple rotors and more unconventional configurations, can be noted in very recent years, e.g. the Bell Nexus and the Airbus CityAirbus. However, the only configuration that is in service, so far, is the V-22 tilt-rotor. This is because the combination of multiple sources of lift and thrust brings significant challenges to the development. In terms of aerodynamics, the interference between the rotary wing systems, lifting surfaces, and the airframe can be significant, depending on the operating condition and their relative positions. In particular, the aerodynamic interference between the rotor systems, such as propulsive propellers under a lifting main rotor, can be notably complex, due to their relative motions, unsteady loadings, and vortical wake systems. The interactions further lead to significant issues such as unfavourable acoustics, large vibration and poor stability, and difficulties in control/trimming. Consequently, the question of optimisation of a configuration to alleviate negative interference effects is raised.

Comparing to conventional helicopters, notably fewer wind tunnel tests of compound configurations, especially thrust augmenting configurations with propulsive rotors, can be found in the public domain. Bain and Landgrebe [3] performed an extensive test campaign on a generalised compound helicopter model in 1967. The tests examined the interactions between the main rotor and wings, and later the main rotor and various propeller configurations. The

tests showed that the effective angle of attack is altered by the main rotor downwash. The bending moments on a tail-mounted propeller blade are larger than the wing-mounted configuration. Both wing-mounted and the tail-mounted propellers increased the main rotor vibratory moments as their thrust was increased. A series of tests on the Sikorsky X2 demonstrator and the later S-97 RAIDER were reported by Walsh and Lorber et.al. [4, 5] in recent years. However, the tests mainly focused on the overall performance, stability and vibration, and limited data concerning the rotor/propeller interaction was disclosed. Bowles et. al. [6] conducted wind tunnel tests on a more generic rotor/propeller model in 2016. They examined the propulsive efficiency and relative vibration levels of a tail-mounted propeller in the wake of a powered main rotor and generic fuselage. The tests found that the propeller had negligible effects on the main rotor performance and trimming, but the propeller performance was significantly altered by the main rotor wake. The propeller efficiency was found increased in the main rotor wake comparing to the isolated condition. The vibration level of the propeller remained similar for the range of propeller positions investigated.

Following the advancement in numerical methods and computational resources in recent decades, high-fidelity Computational Fluid Dynamics (CFD) simulations of compound configurations can also be found. In particular, a series of numerical activities concerning the Airbus X³ and the later RACER configurations recently appeared. Stokkermans et. al. [7] conducted URANS(Unsteady Reynolds-averaged Navier-Stokes) simulations of the RACER configuration, using resolved blades for both lateral propellers and an actuator disk for the main rotor. The study concluded that the aerodynamic interaction mostly happens between the propeller and the wing during high-speed cruise. The propeller efficiency was increased with small overall loading variations due to this interaction, but the single blade loading experienced very large variations. In hover, the propeller was dominated by the main rotor downwash. The blades were operating in the non-linear part of the lift curve with stall observed occasionally, thereby reducing the efficiency. Frey, Öhrle, and Thiemeier et. al. [8–12] also performed high-fidelity URANS simulations of the RACER configuration in trimmed hover, cruise flight, and crosswind, using resolved blades for the main rotor and the lateral rotors, with high-order schemes and mesh adaption. Their work focused largely on the overall performance, acoustics, and flight mechanics, but a systematic isolation of components was also conducted to identify the mutual aerodynamic interferences. Frequency analyses of the lateral rotor thrust fluctuations clearly showed that the propeller thrust is considerably influenced by the main rotor blade passage, and generally more severe aerodynamic interactions were observed on the main rotor advancing side. Overall, these high-fidelity CFD simulations managed to resolved the complicated flow features of the specific configuration in detail, and are very important for the further understanding of the flow physics. However, the computational cost remains excessively high for routine applications, parametric study, and design optimisation. In addition, due to the proprietary geometry used, little can be extracted from these studies in a wider context.

For more generalised configurations, Boisard [13] performed URANS and free wake simulations of a rotor/propeller combination. It was found that propeller thrust sees very low fluctuations when the main rotor wake is passing above the

propeller disk at high advance ratios, but the fluctuations become significant when the main rotor wake is ingested by the propeller disk at lower advance ratios or in hover. The main rotor, on the other hand, saw only very small influences from the propeller. The free wake approach managed to deliver good predictions of the interactional aerodynamics at much reduced computational costs. Similar analyses of compound configurations using lower-order approaches can also be found. Buhler and Newman [14] used a deformable vortex ring model with free wake methods to analyse the performance of a lift-augmenting compound with wings. Parametric study was made to investigate the influence of the wing position, span, angle of attack, and rotor advance ratio. Yeo and Johnson [15] conducted design and aeromechanics investigations of a compound configuration with wings and propellers using the comprehensive tool CAMRAD II. Analyses were made concerning the overall performance, stability, and control. Assessment of the various disk/wing loadings and optimisation of the rotor blade shape were also carried out. However, the results were of limited accuracy with carefully tuned input parameters, as the complex flow physics is beyond the capability of lifting lines and potential flows. Also, as reported by Boisard [13], the stability and convergence may greatly suffer from the strong interactions.

Overall, very few experiments concerning the aerodynamics of compound configurations can be found in the public domain as of now. Modern CFD methods are capable of accurate predictions of the complex flow features, but the computational cost can be excessively high for routine use in design optimisation. Lower-order methods have difficulties predicting the complex and interactional aerodynamics due to their simplified assumptions. Moreover, most existing studies focused on the performance examination of specific configurations. Significant work and research are needed to improve the current understanding of the general flow physics. New tools and approaches striking a balance between the cost and the accuracy are necessary for the systematic investigation and design optimisation of the aerodynamic performance of compound configurations.

In this light, this paper presents both high-fidelity and simplified CFD approaches for investigations of rotor/propeller aerodynamic interactions, as well as, an optimisation framework for compound configurations. The objectives are to demonstrate and evaluate the proposed simulation and optimisation strategies and to provide more insight into the propeller/rotor interactions. High-fidelity simulations of a rotor/wing test case by Leishman and Bi[16] were conducted to validate the in-house HMB3 solver. The computational cost and accuracy of actuator-disk-based modelling of the main rotor were examined and validated against blade-resolved simulations. The actuator disk models were found capable of resolving the complex flow features with reasonable accuracy, and at much reduced computational costs, comparing to blade-resolved simulations. The actuator disk models were then used to model the main rotor in simulations of a generalised rotor/propeller combination [13]. The interactional flow features, and the propeller performance were analysed in detail. Small fluctuations were noted in the overall propeller loading, but very large temporal variations were observed in the single blade loading. A simplified simulation approach, with both the main rotor and propeller modelled by actuator disks, was then evaluated. To quantify the aerodynamic interactions using the simplified model, we proposed an inflow distortion metric through the rotor disk. With the help of the inflow distortion factor and a Kriging surrogate

model, the strength of the interaction with the propeller at different positions under the main rotor was quantitatively visualised. The effects of the main rotor advance ratio, rotor/propeller thrust were also explored. Based on the proposed simplified approach and the inflow distortion metric, optimisation attempts were then made for the relative position of the propeller and the main rotor, i.e. to find the configuration, to minimise the propeller thrust with rolling/pitching moment constraints, using both gradient-based and gradient-free approaches. The derivatives of the propeller inflow distortion with respect to its position were computed through the adjoint method for the gradients-based optimisation. The gradient-free approach used the constructed Kriging model and an Efficient Global Optimisation (EGO) algorithm. Performance of the two optimisation approaches for the current application was assessed, and optimisation results using the simplified models were later examined by blade-resolved simulations. The propeller was found to suffer much less from the main rotor wake and downwash at the optimised position, with much reduced fluctuations in the single blade loading.

II. Numerical Methods

A. HMB3 Flow Solver

High-fidelity CFD methods are used in the present for the accurate prediction of ducted/un-ducted propeller aerodynamic performance and for the fine resolution of the near-field flowfields for further acoustic studies. The in-house Helicopter Multi-Block (HMB3) [17, 18] CFD code is used in the present work. The code has been widely used in simulations of rotorcraft flows [19–22]. HMB3 solves the Unsteady Reynolds Averaged Navier-Stokes (URANS) equations in integral form using the Arbitrary Lagrangian Eulerian (ALE) formulation for time-dependent domains, which may include moving boundaries. The Navier-Stokes equations are discretised using a cell-centered finite volume approach on a multi-block, structured grid:

$$\frac{d}{dt} (\mathbf{W}_{i,j,k} V_{i,j,k}) = -\mathbf{R}_{i,j,k} (\mathbf{W}_{i,j,k}), \quad (1)$$

where i,j,k represent the cell index, \mathbf{W} and \mathbf{R} are the vector of conservative flow variables and residual respectively, and $V_{i,j,k}$ is the volume of the cell i,j,k . To evaluate the convective fluxes, Osher approximate Riemman solver is used, while the viscous terms are discretised using a second order central difference scheme. The 3^{rd} order MUSCL (Monotone Upstream-centered Schemes for Conservation Laws) approach is used to provide high-order accuracy in space. The chimera/overset grid method [23, 24] is extensively used in this work. In the present work, simulations are performed with the $k - \omega$ SST [25] turbulence model.

B. Actuator Disk/Line Models

The actuator disk model is an efficient alternative modelling approach for rotors, based on the momentum theory analysis of rotor disks. It has been widely used as alternative modelling options for edge-wise rotors [26, 27] and propellers [28]. In the present work, the actuator disk model is implemented as equivalent momentum and energy sources injected to the flow-field. The total rotor thrust T is described as follows

$$T = a_x \int_0^{2\pi} \int_{R_{rt}}^{R_{tp}} \Delta P(r, \psi) g(r, \psi, t) \sigma(x, y, z) dr d\psi, \quad (2)$$

where, (r, ψ) are the local polar coordinates on the disk, with the subscripts rt and tp denoting the root and tip values, respectively. a_x is a scaling factor that ensures that the total thrust imposed to the flow-field is equal the amount designated. **Previous studies suggest that the inclusion of tangential loadings only had minor effects on the flow solution but hindered the convergence [29]. Nonetheless, the effects of the tangential loading component were assessed in later sections.**

Here, $\sigma(x, y, z)$ is a disk strength distribution function introduced to help the numerical implementation of actuator disk models. In the current solver, each computational cell is assigned a disk strength σ according to the distance between its cell centre and the designated rotor disk shape. The $\sigma(x, y, z)$ function has the value 1 when the cell centre is exactly on the rotor disk, and quickly reduces to 0 if the cell centre is far away from the disk. The decay follows smooth transitions in both the axial and radial directions, to avoid abrupt discontinuities and to enable the computation of derivatives. In the axial direction, the $\sigma(x, y, z)$ function follows a simple cosine square distribution. The discontinuity at the edge of the rotor disk, where the σ values jumps from 1 to 0, is smoothed out by a sharp half sine distribution.

$\Delta P(r, \psi)$ is the pressure jump distribution function depending on the rotor aerodynamic characteristics. The distribution can be defined in various ways, e.g. from experimental/empirical data, simplified assumptions, or using lower-order tools. In the present work, we used two types of pressure jump functions for simplicity, i.e. the uniform and non-uniform models. The uniform disk model assumes that the rotor thrust is evenly distributed on the rotor disk, resulting in the ΔP being a constant anywhere on the disk. Such a model is suitable for small rotors in axial flight such as propellers. The non-uniform disk model assumes a non-uniform and trimmed loading distribution, depending on the advance ratio, from empirical data of edge-wise flight rotors [30].

The function $g(r, \psi, t)$ is a time-dependent Gaussian. In unsteady simulations, this function redistributes the initial pressure jump to conform with the time-resolved blade shape [30]. This is to resemble the time-resolved blade motions of rotors, thereby allowing more realistic resolution of tip/root vortices systems and further induced aerodynamics. Since it concentrates the momentum sources on the discrete rotor blades, this model is often referred to as the actuator line (AL) approach. In steady simulations, $g(r, \psi, t)$ is set to a constant value of 1.

Equation 2 is nominally evaluated at each computational cell. The thrust value is then converted to equivalent

volumetric momentum and energy sources and added to the discretised governing flow equations. Comparing to blade-resolved simulations of rotors, the actuator disk models resolve fewer flow details due to the lack of accurate geometries/motions, boundary/shear layers etc., but the computational cost is greatly reduced due to the easy convergence and the reduction in grid sizes. The actuator disk models are hence a good option for quick or preliminary studies of complex flow-fields involving rotors, with reasonable accuracy and at much reduced computational costs.

C. HMB3 Adjoint Solver

The adjoint method[18, 31], which is known for its efficient handling of large numbers of design variables with few objective functions, is adopted in the current work to compute the sensitivity of the propeller disk inflow distortion w.r.t its position. Typically, the sensitivity system coupled with CFD methods can be defined as

$$\begin{cases} \frac{dR}{d\alpha} = \frac{\partial R}{\partial \alpha} + \frac{\partial R}{\partial W} \frac{\partial W}{\partial \alpha} = 0, \\ \frac{dI}{d\alpha} = \frac{\partial I}{\partial \alpha} + \frac{\partial I}{\partial W} \frac{\partial W}{\partial \alpha}, \end{cases} \quad (3)$$

where α is the design variable vector. I is the cost function, typically a collection of aerodynamic loads or their combinations. It is a function of $\mathbf{W}(\alpha)$, which is the conservative flow variable vector as in Equation 1. Instead of being independent variables, \mathbf{W} is now subject to design variables α . \mathbf{R} is still the steady state residual vector of the governing flow equations, but is written as a function of $\mathbf{W}(\alpha)$.

The sensitivity system in Equation 3 can be solved directly, i.e. the direct approach. This approach is efficient only when there are far more cost functions than design variables, as the linear system scales with the number of design variables. Alternatively, if there are far more design variables than cost functions, such as in the present work, we can introduce an adjoint vector λ bridging the two terms $\frac{\partial R}{\partial W}$ and $\frac{\partial I}{\partial W}$ as $\lambda^T \frac{\partial R}{\partial W} = -\frac{\partial I}{\partial W}$. The sensitivity system thus becomes

$$\begin{cases} \frac{\partial R}{\partial W}^T \lambda = -\frac{\partial I}{\partial W}^T, \\ \frac{dI}{d\alpha} = \frac{\partial I}{\partial \alpha} + \lambda^T \frac{\partial I}{\partial \alpha}. \end{cases} \quad (4)$$

The linear system hence scales with the number of cost functions and is now irrelevant of the number of design variables. Therefore, the adjoint approach of gradient calculation is especially suitable for aerodynamic shape optimisation. More details about the adjoint formulation in HMB3 and the applications can be found in Refs [18, 32, 33].

D. Kriging Surrogate Model

The Kriging surrogate model [34] is a spatial interpolation method based on Gaussian regression. It predicts the value of an unobserved evaluation point using a distance-based function and a stochastic variance. Comparing to interpolation methods e.g. radial-base function or polynomial approximation, the benefit of Kriging approximation is that it provides not only predictions of function values at unobserved points, but also the uncertainty of the predictions. Kriging has hence been widely used in geostatics and aerodynamic shape optimisation studies. The drawback, however, is mainly the large computational cost. Because for each prediction, a linear system, which scales with the number of sampling points, must be solved.

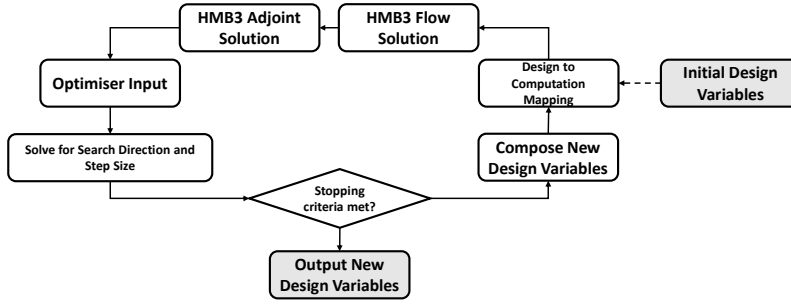
In the current work, the Kriging model was first used to analyse the rotor/propeller aerodynamic interactions, with variations of the propeller position, rotor/propeller thrust ratio, and free-stream velocity. The constructed Kriging model was later incorporated in the gradient-free optimisation framework to optimise the propeller position for minimised aerodynamic interferences. In the present work, the Surrogate Modelling Toolbox of Python [35] is used.

E. Optimisation Methods

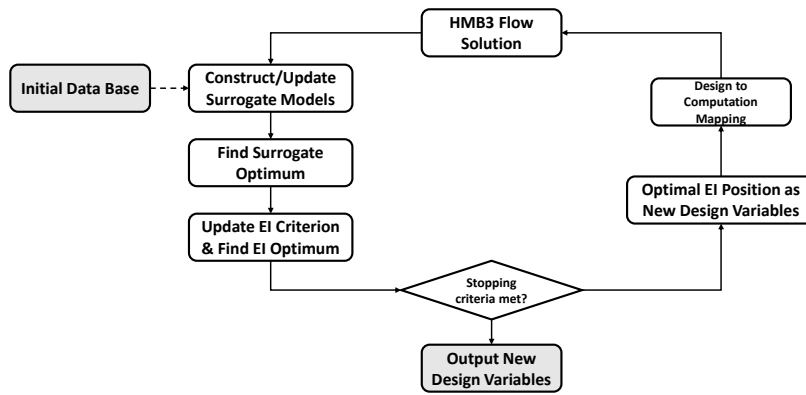
For the optimisation study of the propeller position in the current work, both gradient-based and gradient-free methods were assessed for the optimisation of the propeller position. The gradient-based method, in combination with the adjoint-based gradient computation, is very efficient due to fewer cost function and gradient evaluations, especially when handling large amounts of design variables. However, the optimisation solution may be trapped in local optima due to its gradient-driven nature. It also has difficulties handling discontinuous or non-differentiable objective functions. The gradient-free method, on the other hand, usually leads directly to the global optimal and does not require the computation of gradients. It has no continuity restrictions neither. Nonetheless, it often requires several cost function evaluations at many sampling points. Even with the help of surrogate model representations, the computational cost can be excessive when dealing with large amounts of design variables.

For the gradient-based approach, the Sequential Least-Square Quadratic Programming(SLSQP) algorithm[36] as provided in the *NLopt* library [37] was used here. The framework is shown in Figure 1(a). The SLSQP algorithm solves for the searching direction and step size through a sequence of least-square/quadratic approximations of the objectives functions and linear approximations of the constraints. The design variables are then modified accordingly and new CFD computations are launched to acquire the new cost function value and gradients. The optimisation iterates until the gradients or step size are approaching zero, or the maximum iteration has been reached.

For the gradient-free approach, the Efficient Global Optimisation (EGO) [38] algorithm is used. The framework is shown in Figure 1(b). This algorithm first finds the global optima within the initial Kriging approximation of the cost function and computes the corresponding Expected Improvement (EI) criterion[38]. The EI criterion is evaluated from the uncertainty assessment of the Kriging approximation. This gives a rough indication of the possible improvement



(a) Gradient-based approach based on adjoint computations.



(b) Gradient-free approach based on the EGO algorithm.

Fig. 1 Gradient-based and gradient-free optimisation frameworks.

to the current Kriging optima due to uncertainty. The algorithm then finds the maximum EI, which suggests the best possible improvement, and uses its position in the design space as the next sampling point to launch the CFD computation. The new CFD solution is later added to update the Kriging model and the optimisation loop iterates. The stopping criteria are usually limits on the number of iterations or the value of the EI indicator. Such an algorithm strikes a balance between improving the surrogate accuracy and saving the computational cost, as it only refines the surrogate model locally near the global optima position. To solve for the global optima of the Kriging model and its EI indicator subject to constraints, the classic genetic algorithm as provided in the *pymoo* package [39] is used.

A hybrid approach combining both above methods is also implemented and assessed in the present work. The hybrid approach takes the output of the first few gradient-free iterations as the starting point for the gradient-based approach. This is to avoid the gradient-based approach being trapped in local optima very close to the original design

point. The performance of this approach is evaluated in later sections.

III. Numerical Validation

Ducted propeller in axial flight

To evaluate the performance of the ducted propeller representing rotors in axial flight, a ducted propeller test case by NASA [40] was first adapted here. This ducted propeller configuration has been extensively studied by the authors using high-fidelity, blade-resolved simulations, and detailed information about the geometry, test conditions, and performance can be found in Refs [24, 33, 41]. For the current study, the advance ratio of 0.191 was chosen. At this condition, the propeller disk was carrying about 70% of the total thrust and all the torque with approximately $C_T = 0.036$ and $C_Q = 0.014$.

The current simulations used actuator disk models with simply uniform thrust distributions on grids of about 9 million cells without the blades, which are more than sufficient according to previous grid sensitivity study[24, 33]. The tangential disk loadings, i.e. the torque contributions, were also examined here by introducing a uniform torque distribution. First, comparisons of the duct and centre-body thrust are presented in Table 1. Comparing to the blade resolved simulation, the simple uniform actuator disks gave very close predictions of the duct and centre-body thrust. When the tangential loading was included, the duct thrust predictions were very slightly higher while the centre-body thrust was slightly lower.

Table 1 Duct and centre-body thrust comparisons between resolved blades and actuator disk models at $\mu = 0.191$.

Rotor modelling	Duct thrust/[N]	Centre-body thrust/[N]
Resolved blades	42.29	8.83
Uniform(with tangential loading)	44.73	10.28
Uniform(without tangential loading)	43.52	11.02

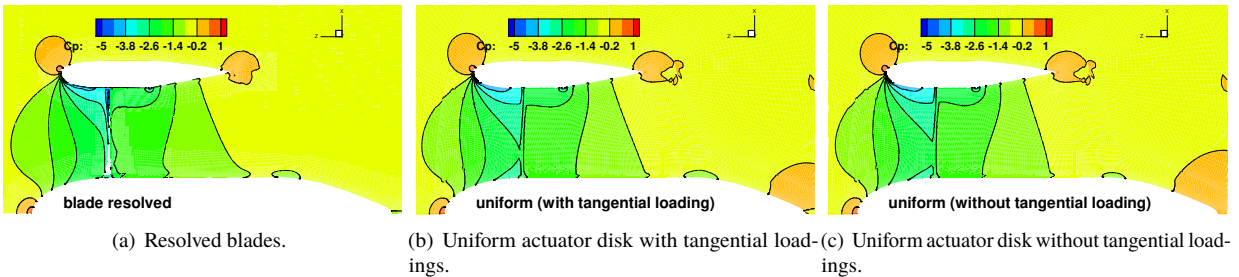


Fig. 2 Time-averaged pressure coefficient contour comparisons between the resolved blades and uniform actuator disk with and without tangential loadings.

Comparisons of flow-fields are presented in Figures 2(a) to 2(c) in terms of time-averaged pressure coefficient

contours, while the time-averaged surface pressure coefficients are presented in Figures 3(a) and 3(b). The uniform actuator disk models induced very similar pressure fields comparing to the blade-resolved simulation. The simplified modelling predicted well the duct surface pressure, and only minor differences were caused by the tangential loading. The differences are mostly limited in regions near the blade root and the centre-body trailing edge. The uniform actuator disks induced larger suction at the blade root. When the tangential loading was included, the pressure at the centre-body trailing edge was reduced because of the swirl velocity and was hence closer to the blade-resolved simulation. Overall, the simple uniform actuator disk model was shown capable of modelling rotors in axial flight with sufficient accuracy, and the tangential loading caused only minor differences.

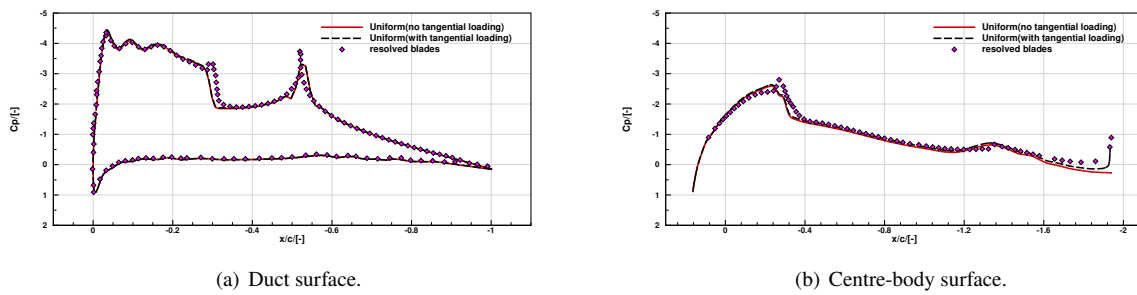


Fig. 3 Time-averaged surface pressure coefficient distributions on the duct and centre-body surfaces using resolved blades and uniform actuator disk with and without tangential loadings.

Rotor/wing Interactions

To verify the actuator disk/line representation for rotors in edgewise flight, a rotor/wing interaction test case by Leishman and Bi [16] was adopted. This test was chosen for the simple geometry, conditions, and the well documented steady and unsteady data. The test configuration consists of a rotor, a lifting surface, and a simplified fuselage, as shown in Figure 4. Details of the geometries can be found in Refs[16, 42]. The experiments varied the advance ratio and the position of the lifting surface, but only limited data was available in the public domain. For the current work, we have selected two advance ratios with the lifting surface on the rotor advancing side, as detailed in the test matrix in Table 2. The rotor trimming data was acquired from previous CFD simulations by Sugawara and Tanabe [42]. Simulations were performed with the rotor modelled using resolved blades, the steady non-uniform actuator disk, and the unsteady actuator line for comparisons. **The actuator disk/line models adopted non-uniform disk loading distributions based on empirical data [30] representing a trimmed edge-wise flight rotor.**

The grid topologies are shown in Figure 4. Grids were generated separately for each component to ensure high quality. The grids were later assembled for computation using Chimera approaches. Uniform grids were used as the off-body grids. Near the main rotor, the cell size were kept at 15% of the rotor blade chord, as recommended by previous grid convergence study by Sugawara and Tanabe [42]. The overall grid for the blade-resolved simulations had about 26

million points. Replacing the blades with actuator disk models reduced the grid size by about 10 million points. The simulations were performed using the 3rd-order MUSCL scheme and the $k - \omega$ SST model. The simulations were performed using 360 time steps for one main rotor revolution. Different time step sizes were examined, but only minor influence on the results were noted. In terms of computational costs for the current simulations, the blade-resolved simulations required about 18 CPU hours for one unsteady time step, while the actuator line approach required only about 3 CPU hours to reach the same convergence level for each unsteady step.

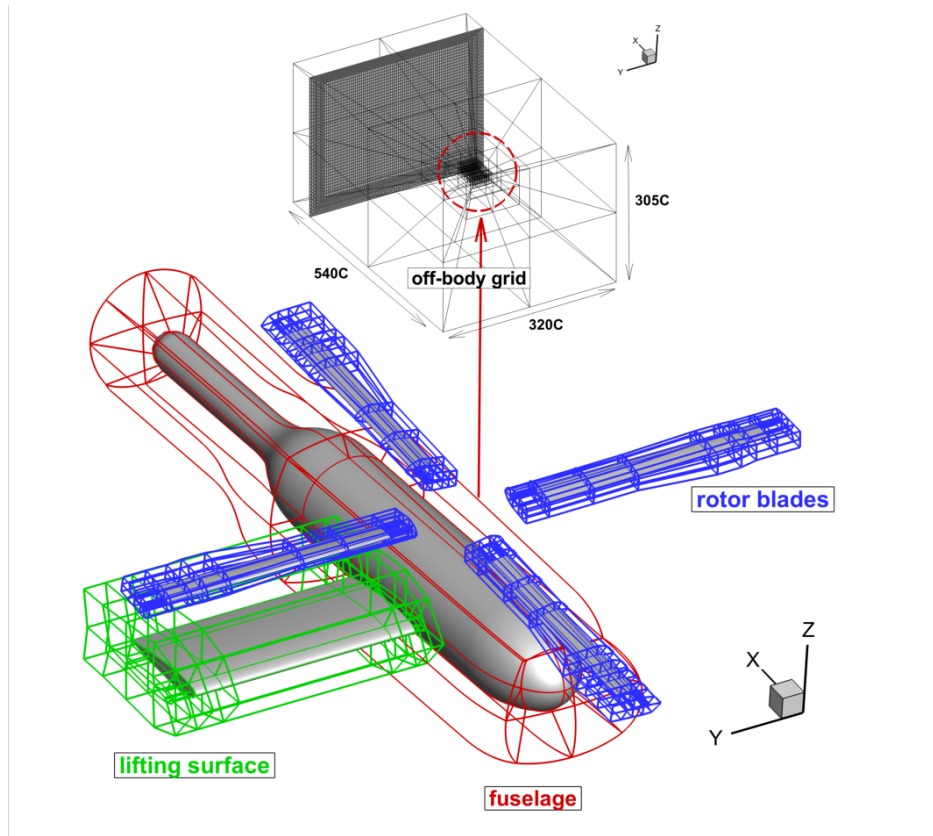


Fig. 4 Geometry and grid topology of simulations of the wing/rotor interaction tests [16].

Table 2 Current test matrix for the rotor/wing configuration by Leishman and Bi [16].

Case Series	Rotor model	Advance ratio	Wing position
1	resolved blades		
2	steady actuator disk	0.075, 0.25	advancing side
3	unsteady actuator line		

Flow details resolved by the unsteady actuator line and the resolved blades approaches are shown in Figures 5(a) and 5(b) at the lower advance ratio of 0.075, and in Figures 5(c) and 5(d) at the higher advance ratio of 0.25, respectively. Comparing to the blade-resolved simulations, the aerodynamic phenomena resolved by the actuator line approach are

very similar. The main aerodynamic features, i.e. rotor tip and root vortex systems, their mutual interactions and interactions with the fuselage and the wing, and the super vortex forming up in the wake, are all resolved with reasonable accuracy by the actuator lines at much reduced computational costs, especially at the higher advance ratio of 0.25. Nonetheless, the actuator line approach is seen incapable of resolving more flow details comparing to the blade resolved simulations, e.g. the blade vortex interactions and the shear layers trailing the rotor blades. Also, it should be noted that the actuator line approach gives lower vorticity magnitudes comparing to the resolved blades, although the shapes of the wake are very similar. This was caused by the lack of boundary layers and shear layers using the actuator line model.

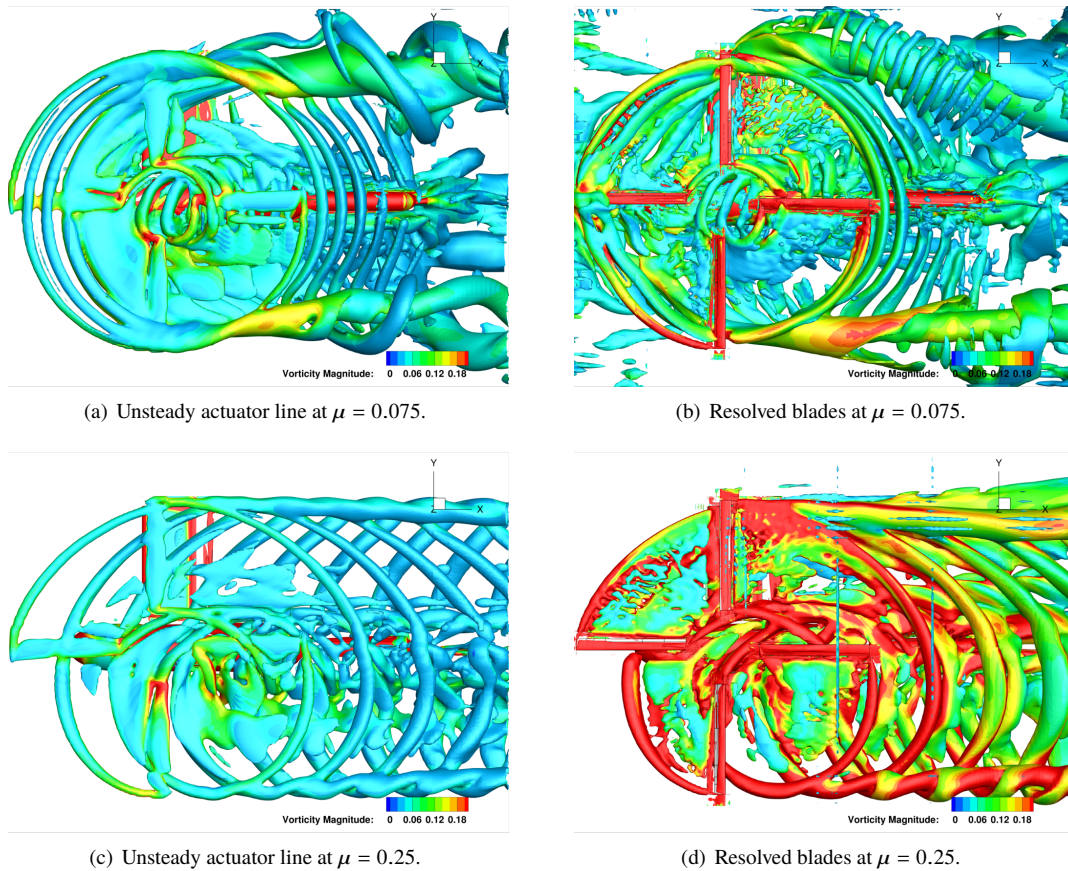
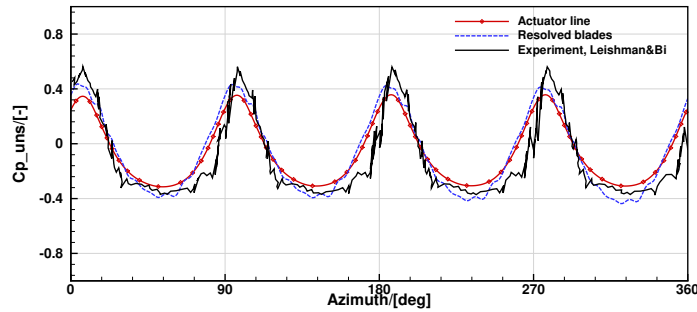


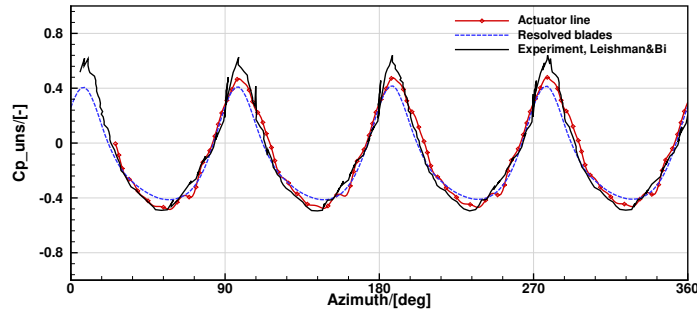
Fig. 5 Iso-surfaces of dimensionless q -criterion = 0.0001 (normalised by tip speed) with actuator line and resolved blades representations at $\mu = 0.075$ and $\mu = 0.25$, coloured with vorticity magnitudes.

More quantitative comparisons, in terms of unsteady pressure signals at a pressure sensor located at 65% span and 11.5% chord on the wing upper surface, are presented in Figures 6(a) and 6(b), respectively for the lower and higher advance ratios. Also presented are the experimental measurements. The experiments [16] recorded pressure fluctuations at several stations on the wing surface at different advance ratios, but only limited data can be found in the public domain. Note that the data shown here have been subtracted by their respective mean magnitude, as small uncertainties in the free-stream pressure cause large shifts in the absolute values of the signal due to the way the data is

normalised. Regardless, our numerical results have shown very good consistency with the test data, in terms of the wave shape, frequency, and magnitude of signals. In general, the blade-resolved signals contain more details and agree better with the test data. The actuator lines resolved the dominant frequencies but filtered out higher harmonic components due to the lack of details in the resolve flow-fields. The actuator lines smoothed out the peaks, because the Gaussian used tends to spread the loads out, and the interaction with the wing is therefore less intense.



(a) Surface pressure signal at $\mu = 0.075$.



(b) Surface pressure signal at $\mu = 0.25$.

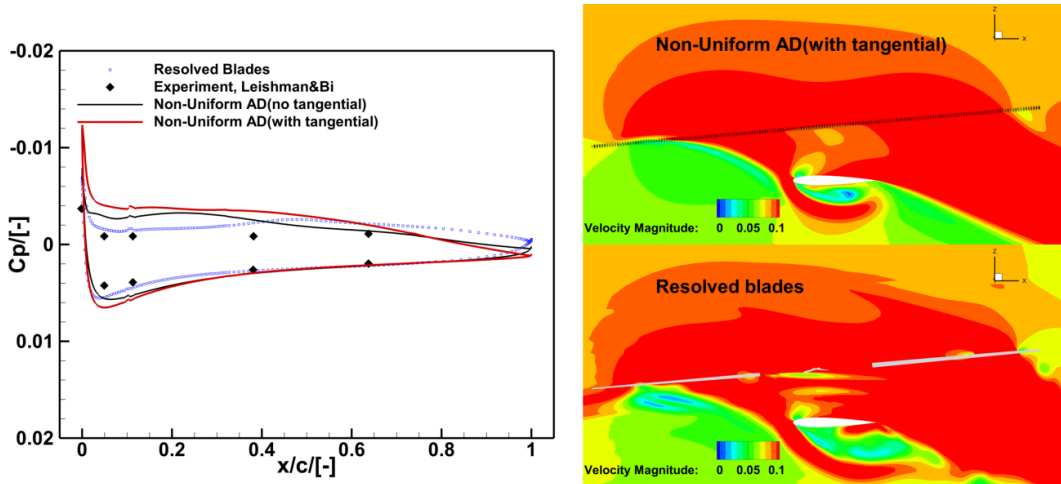
Fig. 6 Comparisons of unsteady wing surface pressure signal variations between simulations and tests by Leishman and Bi [16].

Time-averaged wing surface pressure distributions at 3 wing stations are presented in Figures 7(a) to 7(c), along with comparisons of time-averaged flow features resolved by the actuator disk models and the resolved blades. The influence of the tangential loading component of the actuator disk model was also examined here by adding a uniform torque distribution.

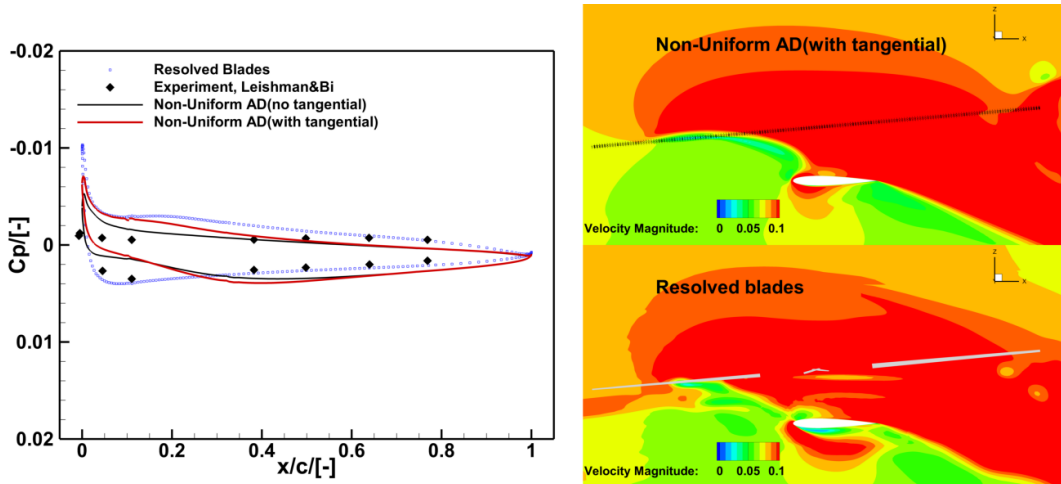
As can be noted from the presented flow-fields, at this low advance ratio of 0.075, a large proportion of the wing lower surface was suffering from excessive flow separation rolling up from the wing leading edge. The resolved blades hence offered better pressure predictions on the wing upper surface at $y/b = 0.3$ and 0.6 . The differences on the wing lower surface were larger due to the inherent limitations of URANS approaches when handling massive separation. Still, the blade-resolved predictions were rather close to the experimental data. At $y/b = 0.8$, the pressure coefficient differences were small and close to zero. Our blade-resolved prediction had reasonable agreement but deviated slightly from the

test data, which was also reported by Sugawara and Tanabe [42] in their simulations. This station is close to the wing tip and is also affected by the rotor tip vortices, hence finer spatial and temporal resolutions may be necessary to resolve the delicate flow details.

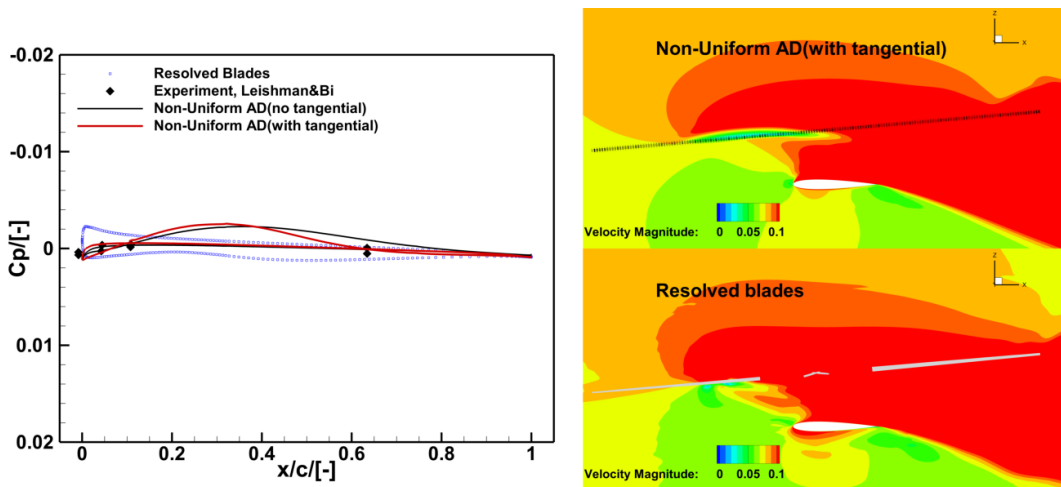
The AD models induced similar flow features as shown in Figures 7(a) to 7(c) comparing to the blade-resolved simulations. In general, the tangential loads brought only marginal improvement to the results due to the inclusion of swirl velocities. The flow convergence, however, was seriously hindered as also have been suggested by Chaffin et. al.[29] Regardless of the tangential loading, the flow separation below the wing was induced properly by the actuator disk models, but the separation region was smaller and ended earlier in the span-wise direction than that of the resolved blades, as shown in Figure 7(b). Still, as a quick and low CPU modelling approach, the actuator disk models offered results with reasonable agreement with test data at this complex condition.



(a) Wing C_p comparisons at $y/b = 0.3$ station.



(b) Wing C_p comparisons at $y/b = 0.6$ station.



(c) Wing C_p comparisons at $y/b = 0.8$ station.

Fig. 7 Wing surface pressure coefficient comparisons between simulations and test data by Leishman and Bi [16].

IV. Numerical Simulation of Rotor/Rotor Wake Interactions

A generalised rotor/propeller combination [13] has been chosen for the investigation of the interactional aerodynamics. The test model consists of a 1/7 Dauphin fuselage, a 1.5-m-diameter main rotor, and a commercial propeller of 11-inch diameter. The propeller had a constant RPM of 7632, while the main rotor rotates at 1272 RPM, resulting in a rotational speed ratio of 6:1. The free-stream velocity varied from 0 to 25 m/s (main rotor advance ratio $\mu = 0.0$ to 0.25), and the thrust ratio between the main rotor and propeller was about 6.3:1. High-fidelity methods are necessary to resolve the interactional aerodynamics, but the largely different spatial and temporal differences between the main rotor and the propeller may lead to excessively high computational costs.

Previous CFD simulations by Boisard [13] suggests that the main rotor sees minor influence from the propeller, whereas the propeller suffers from the main rotor wake and downwash. It is also noted that the main rotor advance ratio plays a significant role in the aerodynamic interactions, as the advance ratio determines the boundary of the wake. At higher advance ratios beyond $\mu = 0.1$, the main rotor wake passes above the propeller disk, inducing only small fluctuations in the propeller thrust. In the intermediate advance ratio range near $\mu = 0.05$, the main rotor wake partially impinges on the propeller disk. The propeller hence sees large influences from the main rotor within certain azimuth ranges. Outside these ranges, the influence is rather small. In hover, the propeller is immersed in the main rotor downwash, and significant fluctuations in the propeller thrust can be noted. Simulations of the hover condition can be very costly due to the lack of free-stream and complex flow details. A low advance ratio of $\mu = 0.05$ was selected because it has significant aerodynamic interactions and requires moderate computational costs for high-fidelity simulations.

Grid topologies used in the current work is shown in Figure 8. Comparing to simulations by Boisard [13] that included only the main rotor and propeller, our simulations also considered an approximated centre-body. The fuselage was also excluded for simplicity. Grids were generated for each component separately to ensure high quality. The grids were assembled for computation using Chimera approaches. The near-field grids had uniform cell sizes near the main rotor and the propeller. In the present study, the propeller blades are fully resolved, while the main rotor is represented by actuator disks or lines, as listed in Table 5. The actuator disk and actuator line models used the same non-uniform disk loading distribution based on empirical data [30]. The tangential loadings were not included for simplicity. The swirl velocities may alter local flow details and complicate the interactions, but their effects are regarded as secondary comparing to the downwash according investigations in previous sections. The simulations were performed using the 3rd-order MUSCL scheme and the $k - \omega$ SST model.

A first study was performed to evaluate the required spatial and temporal resolutions for the current simulation. Grids of different sizes were used as listed in Table 3. Three different time step sizes were also examined, and the test matrix is shown in Table 4. The computations required about 5 to 6 main rotor revolutions, i.e. 30 to 40 propeller revolutions to reach periodic states when modelling the main rotor with unsteady actuator lines. With actuator disks, the

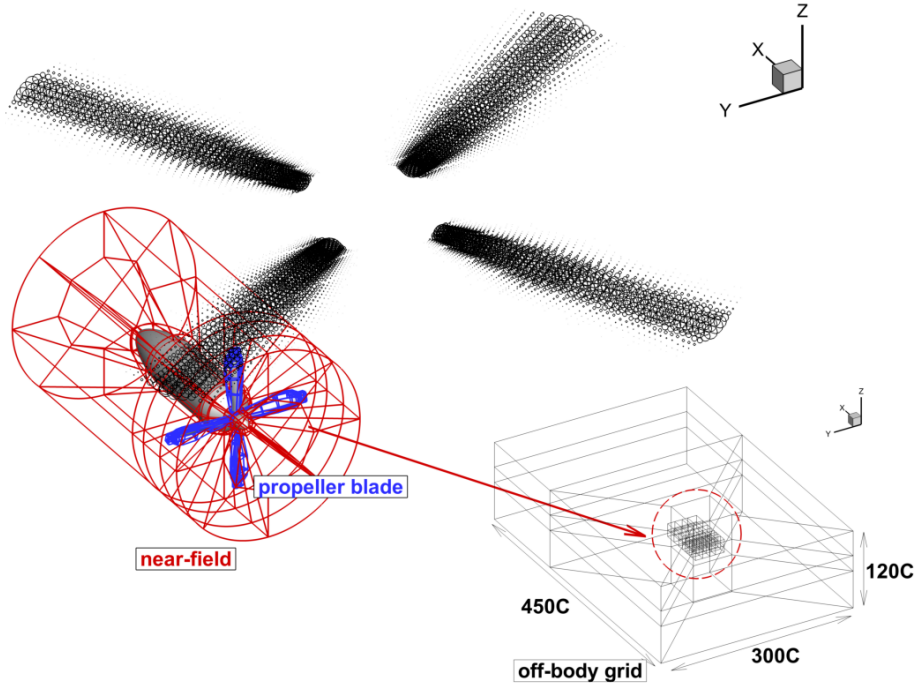


Fig. 8 Grid topology for HMB3 simulations of the rotor/propeller configuration.

computations were less expensive but still required about 10 propeller revolutions to settle. The grid dependence study hence used the larger step size with actuator disks to reduce the computational cost.

Table 3 Grid details for the mesh dependence study of the rotor/propeller interaction simulations.

Grids	Coarse	Medium	Fine
Total cell number/[in million cells]	11.9	18.9	34.1
Near field resolution/[in propeller 75% chords]	0.2	0.13	0.08

Table 4 Test matrix for the spatial and temporal resolution dependence study.

Grid\Propeller step size	$3^\circ/step$	$1^\circ/step$	$0.5^\circ/step$
Coarse	✓	-	-
Medium	✓	✓	✓
Fine	✓	-	-

Predictions of the phase-averaged total propeller thrust and torque using different grids and propeller time step sizes (Table 4) are plotted in Figure 9. In general, the absolute differences were small while using different spatial and temporal resolutions, as the thrust varied within $1.5N$ and the torque differed within $0.05Nm$. The propeller produced a thrust near $20N$ with a torque output near $0.47Nm$. Nonetheless, as can be noted, different grids using the same larger

time step size of $3^\circ/step$ showed minor differences in the thrust and torque predictions. While using the medium grid at different time step sizes, slightly larger changes can be observed when the time step was reduced to $1^\circ/step$ from $3^\circ/step$. The differences between $1^\circ/step$ and $0.5^\circ/step$ remained small.

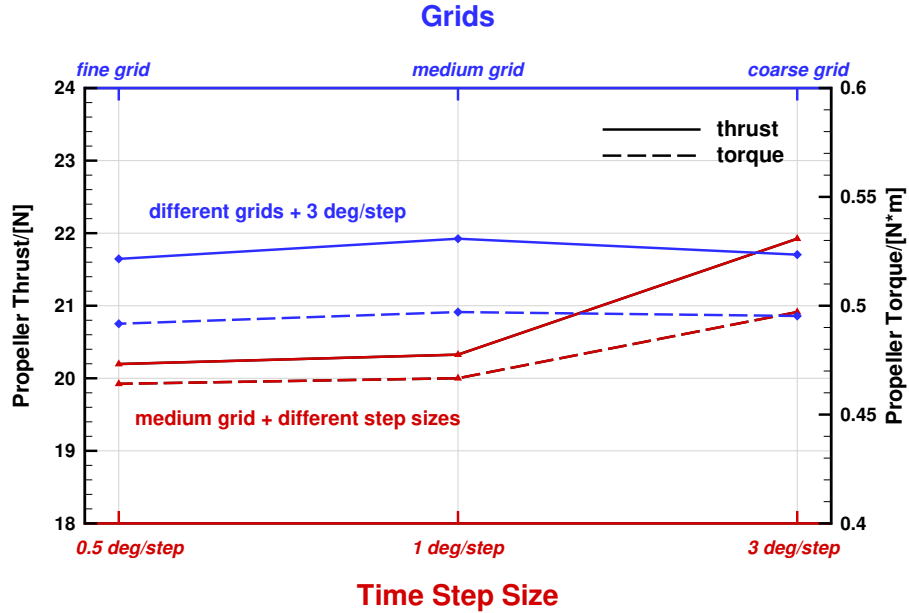


Fig. 9 Examination of grid sizes and propeller time step sizes for the rotor/propeller interaction study.

The test matrix for the rotor/propeller interaction study is presented in Table 5. Simulations of the isolated propeller were first performed for further reference. The main rotor was then modelled with actuator disks or actuator lines. A further simulation was also performed to verify the minimised interactions at an optimised position as detailed in later sections.

Later simulations using actuator disks employed the medium grid with a time step of $1^\circ/step$. However, for simulations using actuator lines, the medium grid and the larger time step of $3^\circ/step$ were adopted. This was mainly due to the computational cost. Because with actuator lines, 5 or 6 main rotor revolutions are necessary for the converged solution, corresponding to 30 to 36 propeller revolutions. Besides, with the resolved main rotor blade motion, to include all the frequencies, one must have flow solutions of at least 1 main rotor revolution, i.e. 6 propeller revolutions. This leads to excessively large computational costs when using finer time steps. To minimise the impact of the step size, the actuator line results were compared with the isolated propeller using the same step size.

A. Blade-resolved Simulations and Analyses of Aerodynamic Interactions

In this section, the propeller was modelled with all blades resolved, while the main rotor was modelled by steady and unsteady actuator disk models since it is less affected by the propeller. Simulations were first performed for the isolated propeller without the main rotor for further reference.

Table 5 Test matrix for the propeller blade-resolved simulations.

Case	Main rotor modelling	Propeller modelling	Propeller position
0	not included(isolated propeller)		initial
1	non-uniform AD	resolved blades	initial
2	non-uniform AL		initial
3	non-uniform AL	resolved blades	optimised

Simulation results using resolved propeller blades (while the main rotor was modelled by a non-uniform actuator disk) are shown in Figures 10(a) and 10(b). The actuator disk provided a constant, but non-uniform downwash. The propeller blades hence experienced non-uniform and non-axial inflows, and the propeller wake was distorted by the downwash. The propeller wake later joined the main rotor wake downstream, forming a strong and complex super vortex structure. The cylindrical centre-body also contributed to the wake due to the downwash.

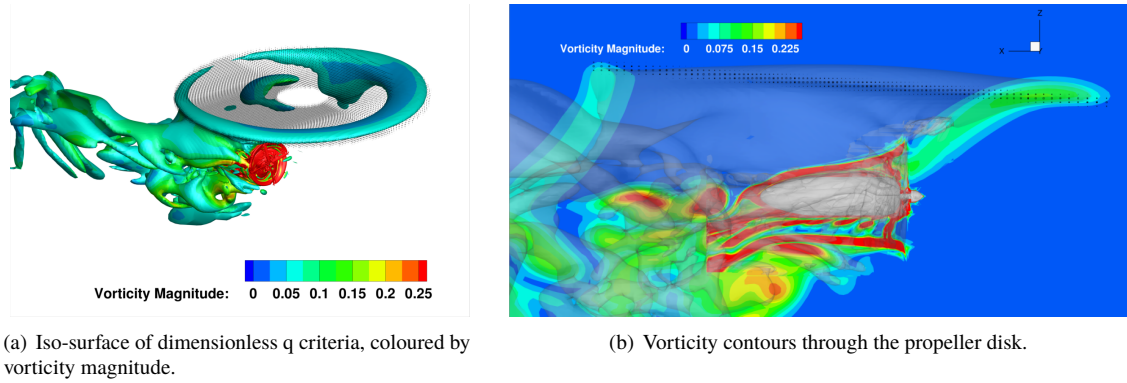


Fig. 10 Flow details of the rotor/propeller wake interactions using resolved propeller blades and steady, non-uniform actuator disk for the main rotor.

Simulation results using resolved propeller blades while the main rotor was modelled by non-uniform actuator lines are shown in Figures 11(a) and 11(b). Comparing to the steady actuator disk approach, the dominant flow features are similar, with the main rotor generating a non-uniform downwash for the propeller and the propeller wake joining the super vortex. However, the actuator lines managed to provide more realistic and complex flow details thanks to the time-resolved blade motion. The tip and root vortices by the discrete blades were resolved, providing time-variant downwash flows for the propeller. Interactions between the propeller and main rotor wakes were also more complex due to the improved flow details.

Phase-averaged integrated aerodynamic loads of the propeller under the main rotor downwash are presented in Table 6. All forces and moments are normalised by the isolated propeller thrust T_0 and Q_0 , respectively, to bring out the relative changes due to the interactions. The subscripts x, y, z denote the Cartesian directions as shown in Figure 8. In general, the propeller in-plane forces were almost negligible compared to the thrust, but the vertical forces were

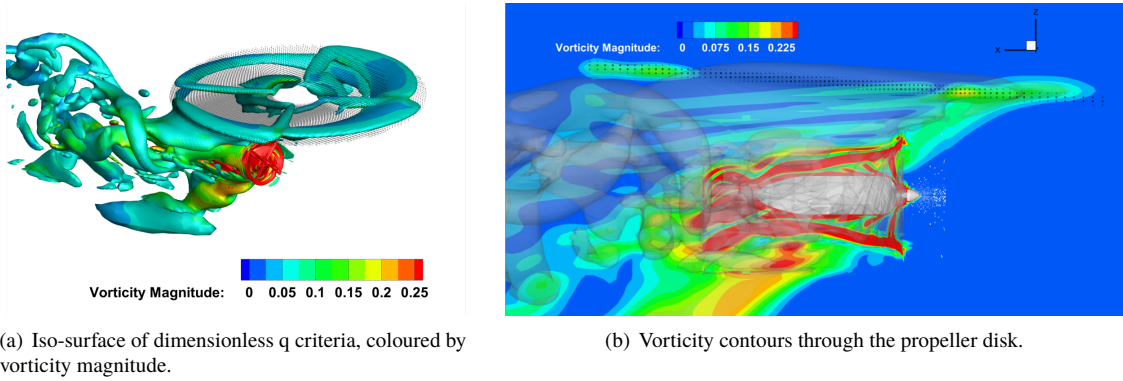


Fig. 11 Flow details of the rotor/propeller wake interactions using resolved propeller blades and unsteady, non-uniform actuator lines for the main rotor.

relatively larger due to the downwash. The disk pitching moment due to the unbalanced disk loading was also negligible, but the yawing moment was much larger.

Comparing the isolated propeller, the actuator disk model predicted a thrust reduction of about 5.5% and a torque reduction of 7%. It should be noted that these corresponded to very small absolute thrust and torque changes of about 1.1N and 0.04Nm, respectively. The predicted thrust and torque reductions agreed well with free-wake predictions by Boisard[13], and the torque reduction also agreed with their blade-resolved CFD simulations[13]. Nonetheless, their blade-resolved simulations predicted a small thrust increase by 1.7%, which differed from the current AD modelling by a small absolute value of about 1.5N. This could be due to factors such as the inclusion of the centre-body. The yawing moment predicted was about 28.6% the propeller torque. The actuator line model suggested an almost unchanged thrust value and a smaller torque reduction by about 2%. It also predicted a smaller disk yawing moment of about 24%. These were due to the slightly lower downwash by the actuator line, as the Gaussian tends to smooth out the pressure jumps.

Table 6 Propeller forces and moments subject to main rotor downwash using different rotor modelling approaches. $T_0 = 21.38N$ and $Q_0 = 0.50Nm$ refer to the isolated propeller thrust and torque.

Case	Condition	F_x/T_0 (Thrust)	F_y/T_0	F_z/T_0	M_x/Q_0 (Torque)	M_y/Q_0 (Pitching)	M_z/Q_0 (Yawing)
1	AD+initial position	94.5%	0.4%	2.2%	92.9%	0.8%	28.6%
2	AL+initial position	100.5%	0.8%	2.3%	98.0%	1.8%	23.7%
3	AL+optimised position	101.2%	0.3%	0.2%	100.6%	0.4%	1.1%

Thrust variations on a single blade due to the non-axial inflow were also extracted as shown in Figure 12(a). The thrust values were also normalised by the isolated propeller thrust T_0 . For the isolated propeller, the blade thrust had a small variation because of mild flow separation at the blade root and interactions with the centre-body. When the main rotor was included either through the steady AD or the unsteady AL, the blade experienced large temporal variations in

the axial force due to the non-axial inflow.

Thrust changes relative to the isolated propeller disk are plotted in Figure 12(b). The loading distribution was obtained by subtracting the isolated propeller loading distributions from the non-uniform actuator disk results. It can be seen that the blade experienced a thrust increase as it is encountering the main rotor downwash between 90° and 180° azimuth angles. The thrust was decreased as the blade leaves the downwash between $\psi = 180^\circ$ and 270° . These also agree well with the single blade thrust variations in Figure 12(a). The imbalanced disk loading also caused the larger disk yawing moment in Table 6. The pitching moment was not so significantly affected as the pitching moment contributions from the thrust changes cancelled out each other. Overall, the interactions affected mostly the upper half of the propeller disk, which is consistent with Figure 10(b) where the main rotor wake mostly penetrated the disk upper half.

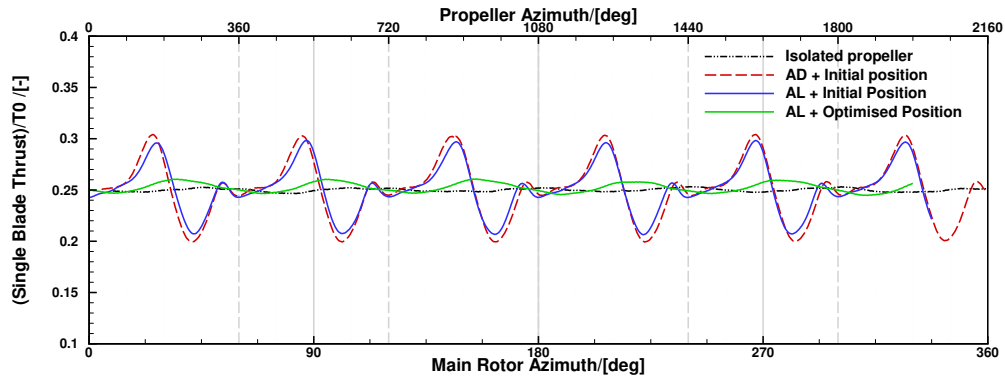
Relative Standard Deviation (RSD) values of the total thrust and the single blade thrust are analysed in Figure 13 to quantify the level of fluctuations. It can be seen in Figure 13 that the total thrust have only small variations less than 1% at the initial position under the main rotor, as suggested by both steady AD and unsteady AL modelling approaches. However, the single blade thrust experienced large levels of fluctuation, around 10%, due to the main rotor interactions. The steady AD brought slightly larger fluctuations, which should be due to the stronger constant downwash.

Fast Fourier Transformations (FFT) of the overall and single blade thrust signals are shown in Figure 14. For the clean propeller, the magnitude of the harmonic components are minor due to the modest temporal variations. Nonetheless, a small peak is noticed at the first propeller BPF (Blade Passing Frequency). Another small peak at the lower frequency should be due to the wake and interactions with the centre-body. For steady AD, the signal shows a strong peak at the first propeller BPF, and a rather weak peak at the second propeller BPF. As for the unsteady AL, several peaks with different magnitudes across the spectrum can be observed. The strongest peak is also the at the propeller BPF, but its magnitude is lower than the steady AD results. The second strongest, which is of about half the magnitude of the first, is at the first main rotor BPF. Other peaks can be observed at the harmonics of either the propeller BPF or the main rotor BPF. **These complex frequency compositions along with the temporal variations in the blade loading may lead to significant vibration and structural concerns.**

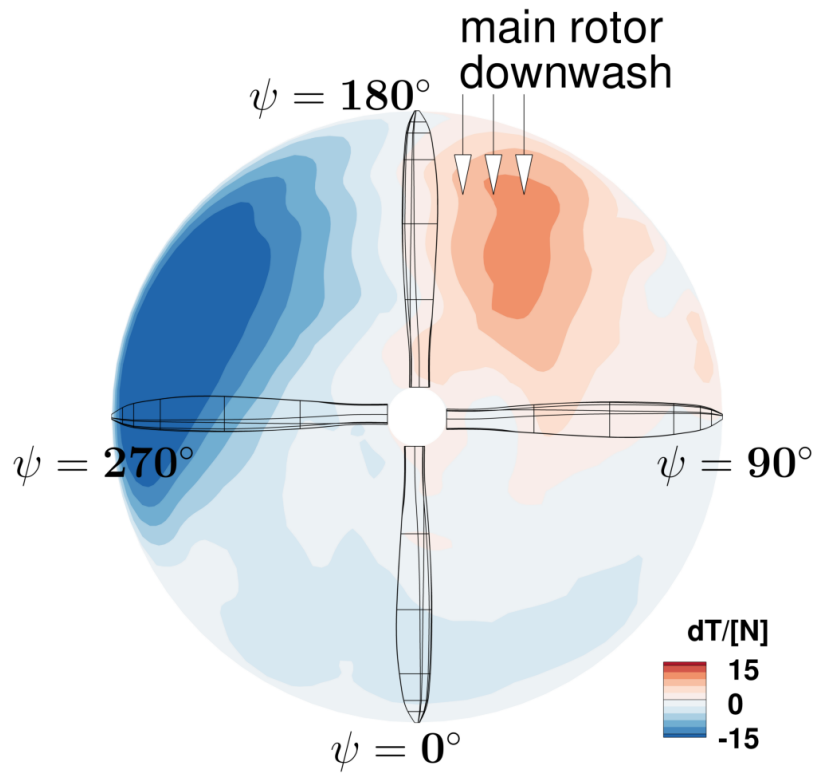
B. Simplified Modelling for Rotor/Propeller Interactions and Surrogate Model Approximations

By representing the main rotor with actuator disks/lines, the computational costs have been greatly reduced comparing to fully blade-resolved simulations. However, this approach can still be costly for parametric investigations or optimisation studies. For faster simulations of the interactional aerodynamics, steady actuator disk models were used to represent the main rotor and the propeller. **The main rotor was modelled by a non-uniform disk using the same empirical data, while the propeller was represented by a uniform disk to balance efficiency and accuracy.**

The implementation and flow details of the actuator disk models is shown in Figures 15(a) and 15(b). The propeller



(a) Single blade thrust variations.



(b) Propeller disk thrust changes relative to the isolated case, with the main rotor modelled by a non-uniform actuator disk. Viewed from downstream.

Fig. 12 Single blade thrust variations and propeller disk thrust changes due to downwash.

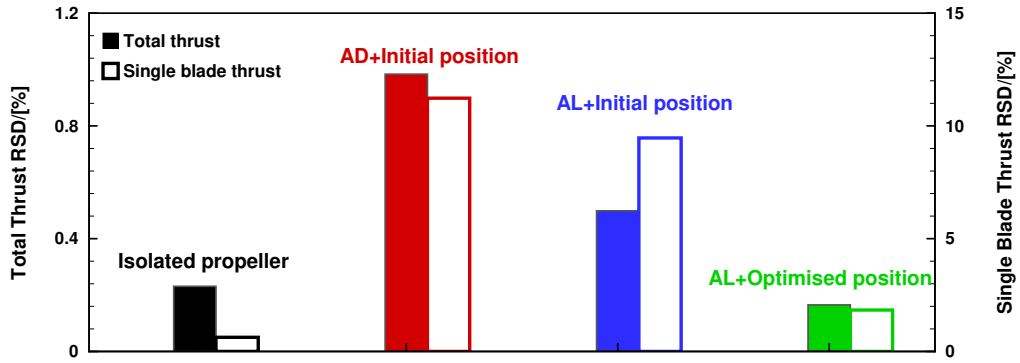


Fig. 13 Relative Standard Deviation (RSD) levels of the total blade thrust and single blade thrust in comparison with the isolated propeller, with different main rotor representations.

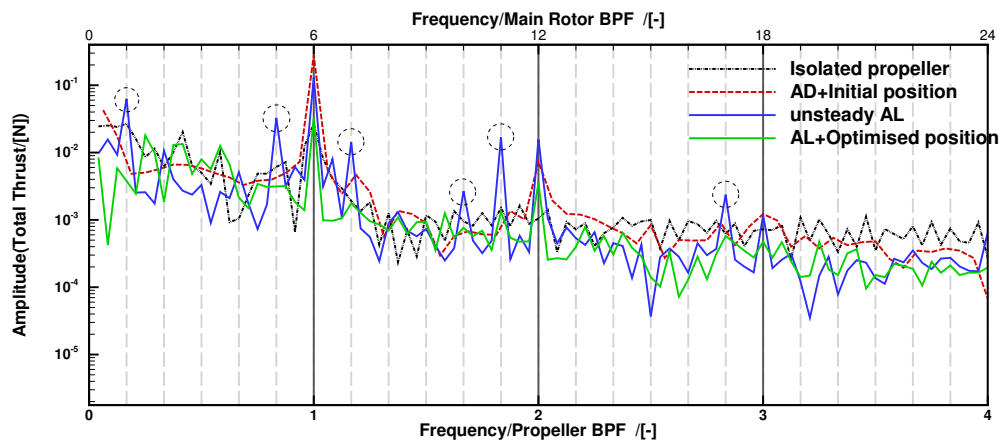


Fig. 14 Frequency component of the overall blade thrust of the propeller in isolation and under the main rotor, with different main rotor modelling strategies.

actuator disk injects momentum and energy into the flow passing through it, thereby accelerating the flow and inducing a pressure jump corresponding to the rotor thrust. **Although the strength of the injected momentum and energy have been prescribed, and changes in the propeller loading due to the aerodynamic interactions have been neglected, the induced flow features are still mostly subject to the non-uniform rotor downwash.** As can be seen from the figures, the main rotor wake is ingested by the propeller disk, and the propeller wake is distorted due to the main rotor downwash. Comparing to the blade-resolved simulations, although many complex flow details have been missed, the dominant flow features in the velocity and pressure fields have been resolved by the simple momentum-based model. On a coarse grid of about 1.5 million cells, with uniform cell size distributions near the disk region, the computational cost using both steady actuator disks is about 5 CPU hours, a huge reduction comparing to the blade-resolved simulations. With such simplifications of rotor modelling, it is enabled to quickly and systematically investigate the interactional aerodynamics with different combinations of rotor position, thrust, advance ratio etc.

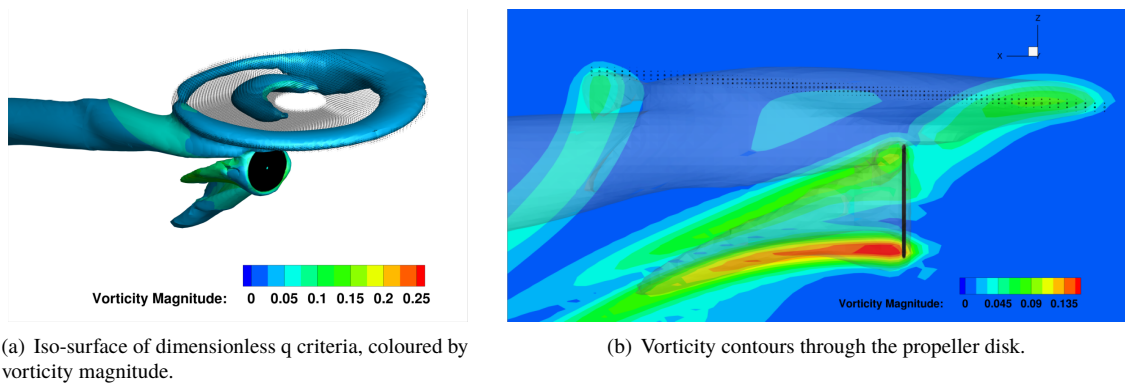


Fig. 15 Flow details of the rotor/propeller wake interactions using steady, uniform actuator disk for the propeller and steady, non-uniform actuator disk for the main rotor. A nacelle was not included for simplicity.

To quantify the aerodynamic interference while using actuator disk models, an inflow distortion factor metric for a rotor disk is defined as follows

$$I_i = \left(1 - \frac{\int \frac{u_i^2}{V^2} dS}{\int dS}\right) \times 100\%, \quad (5)$$

where the subscript i denotes the Cartesian direction of interest, usually the disk axial direction. The integration is carried out over the entire rotor disk plane with dS denoting an infinitesimal disk area element. u_i is the local velocity in the i direction at a disk plane element, and V is the local velocity magnitude. The definition of this metric is rather simple and is linked with the momentum theory analysis of rotor performance. **Essentially, it reflects the proportion of axial speed components in the total velocity passing through the rotor disk plane. A 0% inflow distortion represents an ideal rotor disk that induces velocities only in the axial direction, while a 100% inflow distortion suggests that the rotor disk is completely distorted and is not producing any axial propulsion. Note that an isolated rotor would still have a**

small inflow distortion due to radial/tangential velocities and effects of wake systems, especially when the rotor axial velocity is low. The inflow distortion factor can be normalised by the isolated rotor value to reflect changes relative to the isolated case. It should be pointed out that this definition has ignored axial velocity variations and tangential/radial velocities. Nonetheless, this metric was used because of its effectiveness for the current problem and its simple form, which makes the code implementation and gradient computation especially simple.

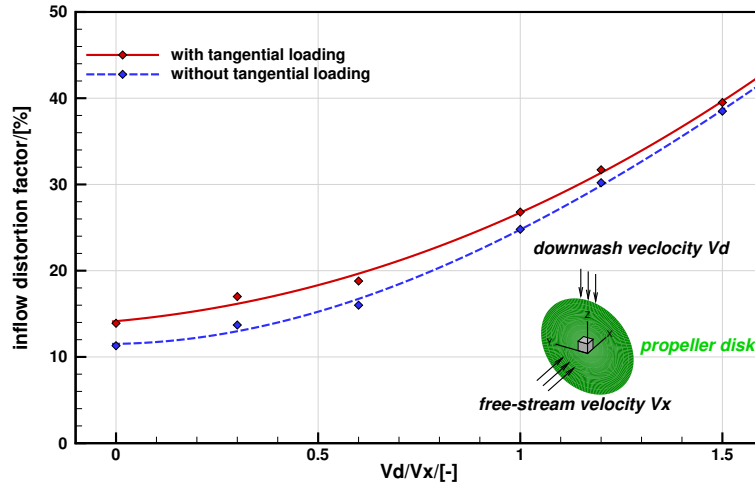


Fig. 16 Variations of inflow distortion factors for a propeller disk at increasing downwash velocities. The propeller was modelled with a uniform actuator disk with and without the tangential loading.

The effectiveness of the proposed inflow distortion metric for propellers operating within downwash is illustrated in Figure 16. The test was performed by introducing an increasing uniform sideways flow velocity for the APC propeller in axial flight at $5m/s$, imitating rotor downwash for propellers. The propeller was modelled using uniform actuator disks with and without tangential loadings. The inflow distortion variations with the increasing downwash velocity are plotted in Figure 16. As can be noted, the distortion factors were low by about 12%, for the isolated propeller with only the free-stream velocity, mainly due to the low axial velocity, the disk in-plane radial velocities and pressure-induced flows at disk edges. With the growing downwash velocity, the inflow distortion increased. When the tangential loadings were included, the inflow distortion factors were about 2% higher because of the tangential velocity component. This difference was small and decreased as the sideways velocity grew, suggesting that the tangential velocity has only secondary effects on the inflow distortion metric.

Using the simplified model and the quantification metric for interactions, we investigated the aerodynamic interactions while the propeller was placed at different positions under the main rotor. The propeller disk was allowed to move within a cuboid region under the main rotor, as shown in Figure 17. For this parametric study, a fully-structured, cartesian grid of about 1.3 million cells was used. The Chimera overset method was used to allow for local refinement for the propeller region of the interest. Within the large cuboid region in Figure 17, a uniform cell distribution of $0.4C$ was ensured in all

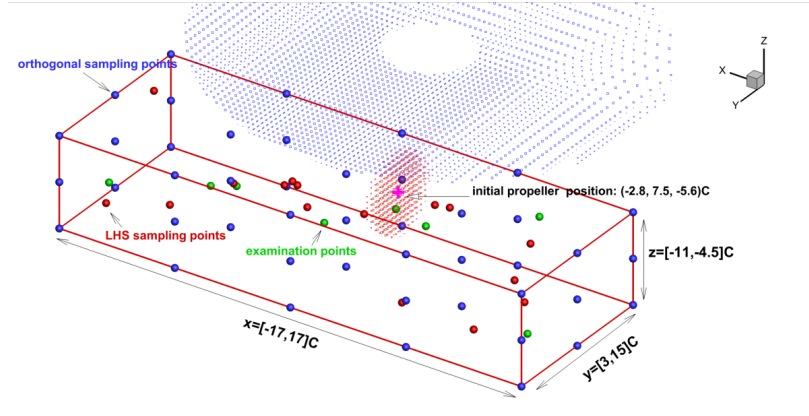


Fig. 17 Boundary of the allowed propeller centre positions under the main rotor. All units are normalised by the main rotor chord.

directions, where C is the main rotor blade chord length. This distribution is fine enough to resolve the dominant flow features since both rotors have been modelled by actuator disks and no wall boundaries are present. The use of this relatively coarse grid for the problem is to strike a balance between the simulation accuracy and the computational cost. The initial HMB3 flow computation using this grid took about 25 CPU hours for very fine convergence, while each successive computation restarting from previous solutions took only about 5 CPU hours.

Several positions were studied, featuring a mixture of orthogonal sampling and Latin hypercube sampling (LHS). 45 orthogonal points ($3 \times 3 \times 5$) and 16 LHS points were initially used. The inflow distortion factors were then computed from the flow solutions. The distortion distribution was considered as a function depending on the propeller position and was then approximated using a Kriging model. The accuracy of the Kriging approximation was examined at 8 extra LHS points plus the initial position, as shown in Figure 18. The Kriging predictions based on 45 orthogonal sampling points are very close to the CFD results. Adding 16 more LHS sampling points improved the accuracy only slightly. These extra points were also added to the Kriging model to further improve the accuracy, amounting to a total sampling of 70 points as also been shown in Figure 17.

The final inflow distortion factor distributions for the propeller and the main rotor disks are shown in Figures 19(a) and 19(b). It can be seen that the maximum distortion for the propeller happened when the propeller was placed downstream and inboard, at the back of the main rotor, around the region where the main rotor wake was passing through. As the propeller was moved further upstream and downwards, the propeller distortion was effectively reduced. As for the main rotor inflow distortion in Figure 19(b), changes in the inflow distortion were very minor responding to propeller offsets. The large inflow distortion was mostly due to the edge-wise flight. Nonetheless, slightly larger distortion was observed when the propeller was placed ahead of and close to the main rotor in vertical direction. This is due to the influence of the propeller wake.

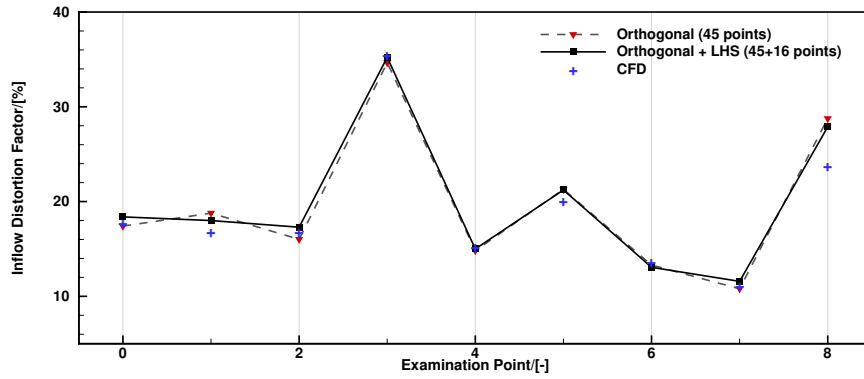


Fig. 18 Validation of the meta-model at an extra 8 Latin hypercube points and the initial point.

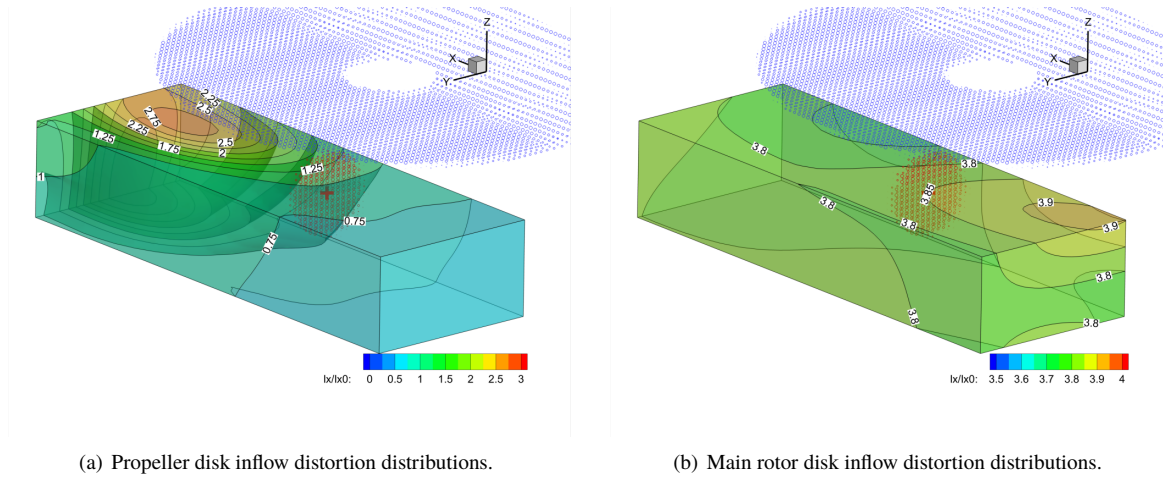


Fig. 19 Kriging models of disk inflow distortion distributions for the main rotor and the propeller while the main rotor is placed at different positions under the main rotor. Values are all normalised by the initial propeller inflow distortion of 17.8%.

C. Influence of Advance Ratio and Propeller Thrust Variations

With the simplified rotor disk representations and the inflow distortion metric, it was straightforward to quickly quantify the aerodynamic interactions at different combinations of operating conditions. This section presents parametric investigations and demonstrations of effects by the main rotor advance ratio and the propeller thrust. A further test matrix was compiled, as shown in Table 7. The main rotor advance ratio varied by changing the free-stream velocity. The propeller thrust was increased or decreased by 50% comparing to the initial case. The same 45 orthogonal sampling set as described earlier was used for each case series to investigate the effects of the propeller position. Kriging models were constructed to approximate the distortion distributions under the main rotor.

Inflow distortion distributions for the propeller at different positions under the main rotor at advance ratios $\mu = 0.025$ and 0.15 are shown in Figures 20(a) and 20(b), respectively. The inflow distortion values were normalised by the initial

Table 7 Test matrix of investigations of the advance ratio and propeller thrust variations.

Case Series	Main rotor advance ratio	Propeller thrust/original propeller thrust
1	0.025, 0.15	1
2	0.05	0.5, 1.5

distortion factor of $I_{x0} = 17.8\%$ while the propeller is placed at the original position with the original advance ratio and thrust.

Comparing to the original advance ratio in Figure 19(a), when the advance ratio was reduced as in Figure 20(a), the maximum distortion region was moved upstream and inboard towards the main rotor root. The maximum distortion value was also increased from about $2.7I_{x0}$ to about $3.0I_{x0}$. Along the longitudinal and lateral directions, the distortion distribution followed a concentric pattern. As the propeller was placed away from the maximum distortion region, either upstream or downstream or outboard, the distortion was reduced. The minimal distortion value was about $0.9I_{x0}$, which is higher than the value at the original position. At the higher advance ratio of $\mu = 0.15$ as in Figure 20(b), the propeller distortion values were overall reduced comparing to the original case. The maximum value was around $0.5I_{x0}$ while the minimal value is about $0.15I_{x0}$. The maximum distortion region was established further downstream and upwards in the vertical direction. The distortion reduced as the propeller was moved upstream and further away from the main rotor vertically. The distortion varied little along the lateral direction.

The propeller disk suffered more severe inflow distortion when it was immersed in or very near the main rotor wake. At low advance ratios, the main rotor wake skew angle was reduced, hence the downwash flow was stronger and covered a larger area under the main rotor. The propeller therefore suffered stronger inflow distortion at most sampling positions under the main rotor. As the main rotor advance ratio was increased, the wake skew angle was increased, and the wake travelled above the propeller disk. Therefore, the overall propeller distortion was reduced, and the maximum distortion was noted only when the propeller was placed downstream and close to the main rotor disk. These also agree well with computations by Boisard[13].

The effect of the propeller thrust is shown in Figures 21(a) and 21(b). It is noted that the propeller thrust changes altered the values but varied little the shape of the distortion distribution comparing to the original case. At the lower propeller thrust (21(a)), the distortion was increased downstream and slightly decreased upstream. At the higher propeller thrust (21(b)), however, the distortion was decreased downstream and slightly increased upstream. These should be due to changes in the relative strength of the propeller suction and the surrounding flow field. The weaker propeller suction made the propeller inflow more dominated by the surrounding flow field. The stronger propeller suction tended to regulate the inflow more along the axial direction, but also induced some distortion especially in uniform flow fields.

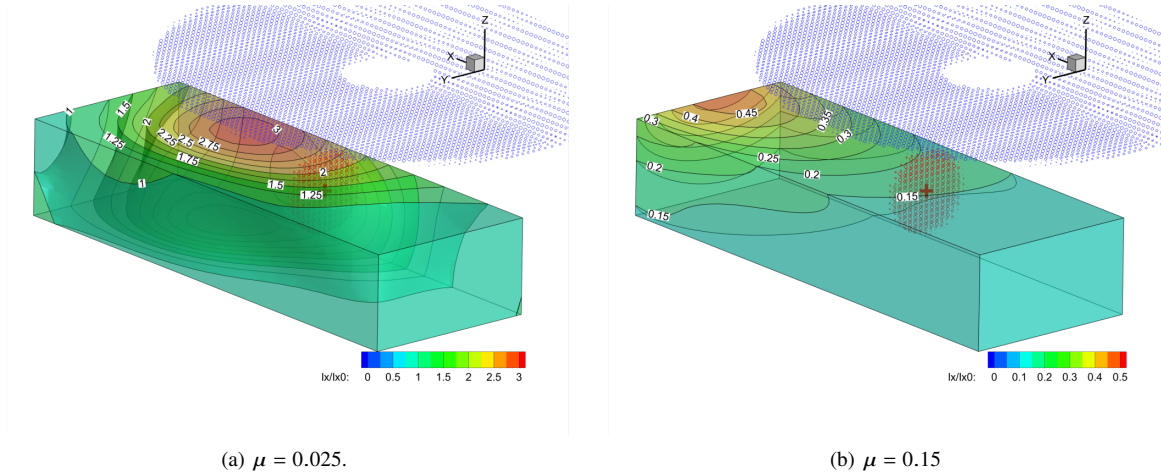


Fig. 20 Propeller inflow distortion variations due to advance ratio changes.

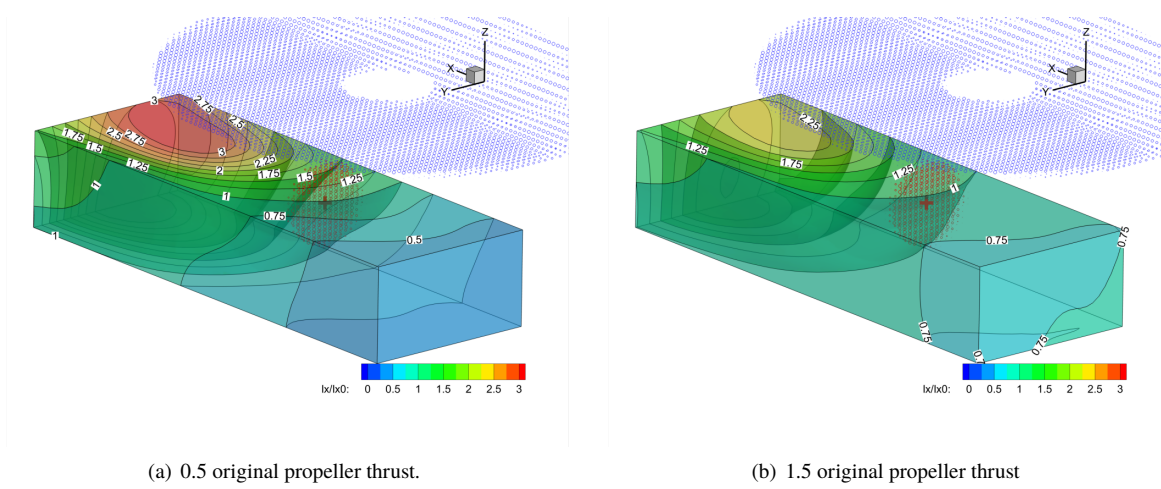


Fig. 21 Propeller inflow distortion due to propeller thrust changes.

V. Minimal Distortion and Propeller Position Optimisation at $\mu = 0.05$

As demonstrated in the previous section, the combination of the simplified rotor modelling and the inflow distortion metric enables quick quantifications of aerodynamic interactions for the propeller under the main rotor. Although at reduced accuracy, the results can be used to guide and improve the configuration design of novel rotorcraft. It is hence of interest to build an extra framework to help locate lower distortion regions and find optimal propeller positions subject to constraints. **The advance ratio of $\mu = 0.05$ was again chosen as a typical condition with significant aerodynamic interactions, moderate costs, and simple operating conditions to demonstrate the proposed optimisation frameworks.**

A. Finding minimal distortion

The first attempt was to simply locate the minimal propeller distortion and the corresponding propeller position at the advance ratio of $\mu = 0.05$. To find the minimal distortion, both gradient-based and gradient-free methods were

evaluated. A hybrid approach was also examined using the approximated minimal by the meta-model as the initial point for the gradient-based approach. This is essentially a non-linear optimisation problem, with the cost function being the propeller distortion factor and the design variables being the propeller position, and with only design variable boundary constraints.

The gradient-based method drives the propeller position changes based on the gradient information of the distortion factor w.r.t the propeller position. The gradient-free method uses the constructed surrogate model approximation and finds the minimal using the EGO algorithm [38]. The gradient-based approach is often more efficient, especially handling large amounts of design variables, but the final solution may be a local optimal rather than the global due to the gradient-driven nature of the method. The meta-model-based approach offers the global optimal, but it requires a large number of cost function evaluations. When dealing with large numbers of design variables and combining with CFD methods, the computational cost can be excessively large. To combine the advantages of both methods and avoid their respective drawbacks, the proposed hybrid approach launches the gradient-based optimisation from an initial guess of the global optimal provided by the meta-model. This section presents the evaluation of all approaches by setting them to find the minimal distortion.

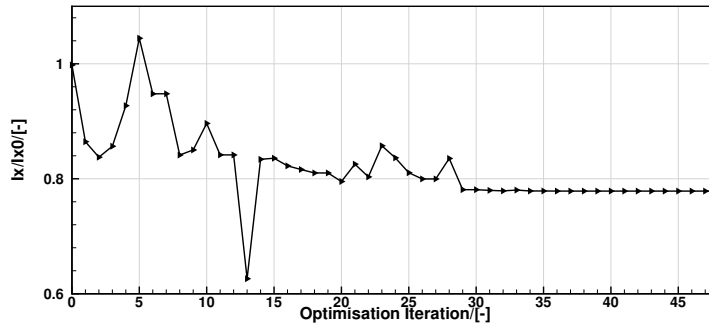
As described in previous sections, we computed the gradients of the cost functions w.r.t the design variables through the adjoint approach. The gradient computation was validated against finite difference results as shown in Table 8. The agreement between the adjoint computation and the finite differences are very good despite the small absolute values. The gradients were then fed into a Sequential Least-square Quadratic Programming (SLSQP) [36] optimiser, which was used to govern the optimisation process.

Table 8 Validation of the adjoint-based computation of raw gradients using finite differences at the initial propeller position.

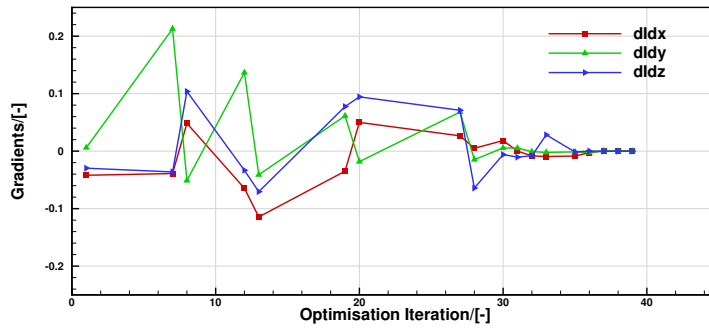
Variable	Finite differences	Adjoint gradients
x	-2.38E-03	-2.65E-03
y	-1.99E-01	-1.99E-01
z	-1.14E-02	-1.01E-02

The convergence history of the cost function values and gradients are shown in Figures 22(a) and 22(b), respectively. The cost function values varied little since the 29th iteration, while all the gradients approached zero after about the 35th iteration. Note that the SLSQP optimiser only occasionally requires the gradient information to construct its own quadratic approximation.

For the gradient-free approach, we used the constructed Kriging model, using a total of 70 sampling points as described earlier, as the initial surrogate model. The EGO algorithm, described in the previous sections, was used here to govern the minimisation process. The convergence history of the EI criterion is presented in Figure 23. The EI



(a) Convergence history of the distortion factor.



(b) Convergence history of the gradients.

Fig. 22 Convergence history of the gradient-based propeller disk position optimisation.

criterion varied little after the 10th iteration.

The hybrid approach started from the initial guess provided by the Kriging model, using 70 sampling points. Its convergence was very similar to that of the gradient-based approach, but with fewer number of iterations. It converged within 25 iterations with all gradients approaching 0.

Detailed comparisons of the three approaches to find the minimal propeller distortion position are presented in Table 9. In terms of the computational cost, the gradient-based required 50 flow evaluations and 20 gradient evaluations. Note the adjoint computation if of the similar size of the flow computation using about 5 CPU hours. The total computational cost is hence about 373 CPU hours. For the gradient-free approach, 92 flow evaluations were invoked taking into account the initial CFD data base. The computational cost is about 491 CPU hours. The hybrid approach based on the initial 70 flow computations, invoked a further 25 flow evaluations and the 13 adjoint computations, the computational cost is about 572 CPU hours.

In terms of minimising the interference, the gradient-based approach very slightly moved the propeller disk upstream and downwards in the vertical direction to $(-4.30, 7.43, -6.02)C$. The reduction in inflow distortion relative to the initial position was only about 22%. However, it should be noted in the cost function history in Figure 22(a), the distortion factor at optimisation iteration 13 was much lower than the final solution. Yet the gradient history in Figure 22(b)

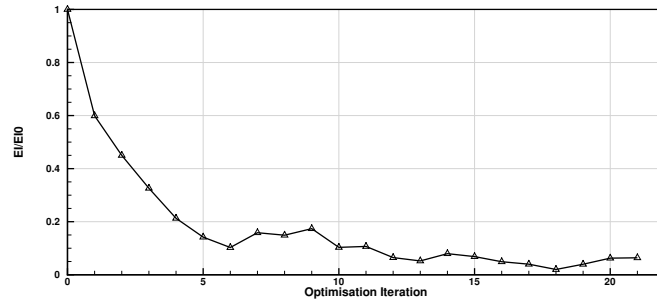


Fig. 23 Convergence of the EI (Expected Improvement) criterion for the gradient-free minimisation, values normalised by the EI value of iteration 0.

suggests that the final solution was indeed an extremum of the objective function, as the gradients were all approaching zero, suggesting that the final converged solution was a local minimum. As for the gradient-free approach, the propeller disk was moved to $(-17.00, 14.35, -5.03)C$, reaching the design variable boundary in the lateral and longitudinal directions and placed further upstream and outboards. This agrees well with the Kriging approximation in Figure 19(a) and the distortion factor varied little in the vertical direction near the minimal position. The relative reduction was about 38% relative to the original. Using the hybrid approach, the propeller disk was moved to $(-13.09, 8.10, -11.00)C$, and the disk inflow distortion was reduced by about 34%. Comparing to the gradient-free approach, the hybrid approach was again trapped in a local minimal in the present application. This also suggests that the current unknown objective function is hilly, and gradient-free approaches are hence more suitable for the optimisation study. However, comparing to the initial gradient-based method, the hybrid approach brought much improved results. The larger computational cost was mostly due to the initial data base for the Kriging model.

Table 9 Comparisons of the gradient-based and gradient-free approaches to find the minimal propeller distortion position.

Approach	Computational cost			Minimal distortion solution	
	Flow evaluations	Gradient evaluations	Total CPU hours	Propeller position	Normalised inflow distortion I_x/I_{x0}
Gradient-based	50	20	~373	$(-4.30, 7.43, -6.02)C$	78.1%
Gradient-free	70+22	0	~491	$(-17.00, 14.35, -5.03)C$	61.7%
Hybrid	70+25	13	~572	$(-13.09, 8.10, -11.00)C$	66.5%

Overall, it is shown that at the advance ratio of $\mu = 0.05$, to minimise the interaction with the main rotor, the propeller should be placed upstream and outboards, to avoid the main rotor downwash and wake. The vertical direction showed minor influence near the minimal distortion position in the current study. In fact, it should also be noted that the absolute inflow distortion value varied little, generally between 11% and 13%, for the region with $X < -12C$. In other words, the aerodynamic interaction would be a relatively small concern in that region, and more design freedom is allowed if the propeller is placed within this region. The gradient-based approach clearly showed an advantage in saving

the computational cost, but the solution was trapped in a local minimum because of the hilly objective function space. The gradient-free approach is hence more suitable for the optimisation study for the current problem.

B. Propeller position optimisation

Optimisation of the propeller position to minimise inflow distortion, was later attempted with constraints imposed at the advance ratio of $\mu = 0.05$. The gradient-free, EGO approach was chosen for optimisation after above evaluations. The optimisation involved only the main rotor and the propeller, both were represented by actuator disk models as described in previous sections. Throughout the optimisation process, the main rotor thrust was kept constant to balance the total weight. The propeller thrust was also kept the same, assuming only minor changes in the total drag while the propeller was placed at different positions.

Constraints for the current optimisation were set to restrict changes in the overall moment. This is because changes in the propeller position alter the centre of gravity of the overall configuration, depending on the ratio of the propulsor unit weight to the total weight. With the centre of gravity moved, the moment arms of other aerodynamic components are also changed. With the current constraints, while optimising the propeller position for reduced aerodynamic interference, trimming changes brought to the original configuration were also constrained.

The optimisation problem was formulated as follows

$$\begin{aligned} &\text{minimise: } I(x, y, z, W), \\ &\text{subject to: } dM_{x_{total}} = 0, \\ &\quad dM_{y_{total}} = 0, \\ &\quad x_{il} \leq x_i \leq x_{iu} \end{aligned}$$

where $I(x, y, z, W)$ is the inflow distortion factor for the propeller disk subject to its centre position (x, y, z) and the flow solution W . $dM_{x_{total}}$ and $dM_{y_{total}}$ are the changes in the overall rolling and pitching moments due to the propeller position change, respectively. These two are imposed as equality constraints for the current optimisation problem. Overall, the optimisation is set to minimise the propeller distortion by altering its position while introducing only minor changes in the overall rolling and pitching moments. In the current work, the initial CG position was assumed at $(0, 0, -3.842)C$ relative to the main rotor centre of rotation, thereby generating zero initial rolling and pitching moments. Throughout the optimisation, we assumed that the propulsor unit to total weight ratio is 5%.

Comparisons between the initial and the optimisation results are shown in Table 10. The optimisation converged after just 3 extra flow evaluations with the EI reaching zero, since the search direction has been largely restricted by the moment constraints. With the constraints imposed, the optimisation also moved the propeller propeller upstream and downwards, but the offsets were restricted comparing to the unconstrained case in Table 9. At the optimised position,

the inflow distortion is about 71.3% of the original, a reduction by about 29%. The rolling and pitching moments were maintained near zero by the constraints at the optimised positions.

Table 10 Optimisation results using gradient-free EGO with overall moment constraints. Moments are normalised by the initial overall torque (Z moment) M_{z0} , and distortion factors are normalised by the initial distortion factor I_{x0} .

Case	dM_x/M_{z0}	dM_y/M_{z0}	Propeller position	I_x/I_{x0}
Initial	0.00E+00	0.00E+00	(-2.80, 7.50, -5.60)C	100%
Optimised	1.07E-04	-3.29E-05	(-10.39, 7.50, -8.28)C	71.3%

Optimisation results using the simplified modelling were later verified through blade-resolved simulations. As shown in Figures 24(a) and 24(b), the propeller disk is now free from the main rotor wake at the optimised position. The interactions mostly happened in the propeller wake far downstream. **The integrated blade loadings are also listed in Table 6. Comparing to the isolated propeller, the overall thrust and torque were recovered to the original levels at the optimised position. The propeller in-plane forces and out-of-plane moments were also negligible due to the reduced interference.** The single blade thrust is presented in Figure 12(a) and the thrust fluctuation levels are shown in Figure 13. Comparing to the isolated propeller, the total thrust variation levels were similar and small below 1% at the optimised position, but the single blade thrust fluctuations were still larger due to the interaction at about 2%. However, comparing to the original position, the fluctuation levels were greatly reduced. Frequency analysis of the total thrust was also conducted and shown in Figure 14. At the optimised position, the propeller thrust had mostly the propeller BPF and its harmonics, suggesting only minor influence from the main rotor. Overall, the optimisation through the simplified models using actuator disks effectively reduced the interference to the propeller disk.

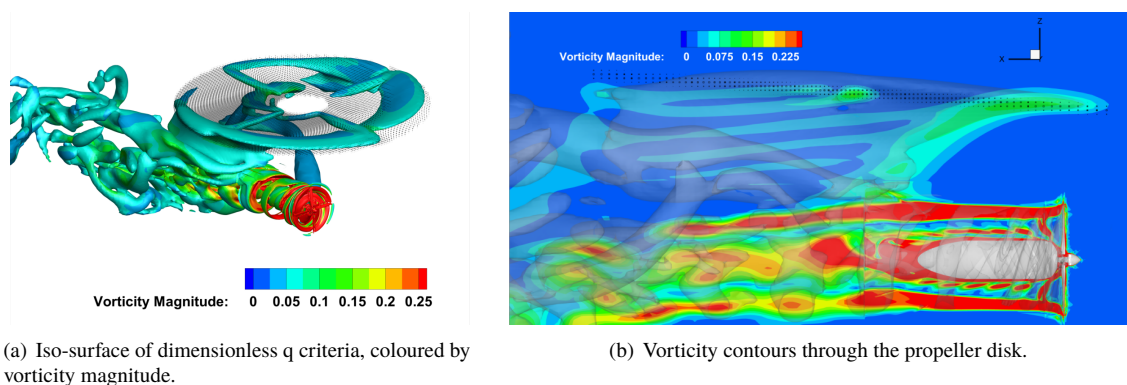


Fig. 24 Flow details of the rotor/propeller wake interactions using resolved propeller blades and unsteady, non-uniform actuator lines for the main rotor, with the propeller at the optimised position for minimal inflow distortion.

VI. Conclusions

This work presented both high-fidelity and simplified CFD approaches for the simulation of the rotor/propeller aerodynamic interactions for compound configurations. An optimisation framework to minimise the interference between the rotor and propeller was also proposed, and its effectiveness and efficiency were demonstrated. From the current investigation, the following conclusions can be drawn:

- 1) The actuator disk (AD) or actuator line (AL) modelling of rotors in axial or edgewise flight can deliver flow predictions with reasonable accuracy at much reduced computational costs. The AD and AL modelling approaches were carefully examined and compared with blade-resolved simulations. For the ducted propeller in axial flight, the uniform actuator disk modelling brought quite accurate predictions of duct thrust and flow details. For the wing/rotor interaction case, the AD and AL modelling brought reasonably accurate predictions of steady and unsteady pressure fields, as well as, the flow details including the excessive flow separation below the wing. The tangential disk loading was found having limited improvements on the results, but the flow convergence was hindered because of the inclusion of swirl velocities.
- 2) For the current rotor/propeller combination at the low advance ratio of $\mu = 0.05$, the aerodynamic interactions between the propeller and rotor mainly affect the propeller performance, especially the upper half of the propeller disk. The propeller blade experienced a thrust increase when encountering the downwash near $\psi = 150^\circ$, and a thrust decrease near $\psi = 210^\circ$. Frequency analyses show that the loading variation consists of strong high-frequency components corresponding to the propeller rotation, and relatively weak low-frequency components corresponding to the main rotor blade passage. The time-averaged total propeller thrust and torque varied little in terms of absolute values because of the interactions. The relative changes, however, were larger because of the small baseline values. The AD model predicted a thrust decrease by about 5.5%, as well as, a torque decrease by about 7%. The AL model predicted an almost unchanged thrust and a slightly reduced torque by about 2%, which should be due to the weaker downwash induced. Both models predicted negligible disk in-plane forces and a slightly larger disk yawing moment of about 28% the torque because of the imbalanced disk loading. Nonetheless, larger temporal variations in the total and single blade loading signals were seen due to the downwash, which were consistent between the AD and AL modellings. Fluctuation levels of total thrust were generally within 1%, while the single blade thrust varied about 10% about the mean values.
- 3) The simplified modelling of rotor/propeller aerodynamic interactions using actuator disks can effectively model the interactional aerodynamics with reasonable accuracy and at much reduced computational costs. The proposed inflow distortion metric is able to quantify the aerodynamic interference for rotor disks in edgewise flow, such as propellers under main rotors. With the help of the Kriging surrogate method, the strength of the interaction at different propeller positions under the main rotor was visualised, with variations in advance ratios and propeller thrust. The propeller experienced larger interference when immersed in the main rotor wake. The shape of

the high-interference region is cylindrical with a skew angle, reflecting the shape the main rotor super vortex through the region. The propeller inflow condition is effectively improved when moved away from the main rotor wake, either upstream/downstream or inboard/outboard. The simplified modelling effectively reflected changes of the main rotor wake due to the advance ratio and the corresponding changes in the interference. Stronger propeller thrust or suction leads to reduced interference from the main rotor and vice versa, but the shape of the interference region is mostly determined by the main rotor advance ratio.

- 4) Optimisation studies based on the simplified modelling are performed at $\mu = 0.05$ to minimise the interference for the propeller by changing its position under the main rotor, with constraints on changes in the overall rolling/pitching moments. Gradient-based optimisation, gradient-free optimisation, and a hybrid approach combining both are evaluated. The employed objective function was found to be hilly with many local optima, hence the gradient-free approach was chosen for the optimisation. The optimisation moved the propeller upstream in the longitudinal direction and downwards in the vertical direction to escape the main rotor wake, with minimal changes in the overall rolling and pitching moments. The optimisation result was later verified using blade-resolved simulations. Fluctuations in the blade thrust were effectively eased at the optimised position, with the single blade thrust fluctuating around 2%, and the disk out-of-plane moments were also eliminated, suggesting a much reduced aerodynamic interference.

This work is a first step towards high-fidelity optimisation at vehicle level. Future work will continue to **improve the definition of the inflow distortion matrix to reflect axial velocity variations, and employ more advanced actuator disk models**, and apply the simplified modelling and optimisation to more complex configurations with multiple rotor systems.

Funding Sources

The sponsorship of the University of Glasgow and the China Scholarship Council is gratefully acknowledged.

Acknowledgments

The HPC service of ARCHIE-West, ARCHER2, Cirrus is appreciated. The authors also wish to thank Professor J Gordon. Leishman for sharing his experimental data and the GATEUR AG25 group for the useful discussions on interference.

References

- [1] Orchard, M., and Newman, S., “The fundamental configuration and design of the compound helicopter,” *Proceedings of the Institution of Mechanical Engineers, Part G: Journal of Aerospace Engineering*, Vol. 217, No. 6, 2003, pp. 297–315. <https://doi.org/https://doi.org/10.1243/095441003772538570>.

- [2] Ormiston, R. A., “Revitalising advanced rotorcraft research - and the compound helicopter ,” *The Aeronautical Journal*, Vol. 120, 2016, pp. 83 – 129. <https://doi.org/https://doi.org/10.1017/aer.2015.5>.
- [3] Bain, L. J., and Landgrebe, A. J., “Investigation of compound helicopter aerodynamic interference effects,” Tech. rep., United Technologies Corp, Stratford CT, Sikorsky Aircraft Div., 1967.
- [4] Walsh, D., Weiner, S., Arifian, K., Lawrence, T., Wilson, M., Millott, W., and Blackwell, R., “High Airspeed Testing of the Sikorsky X2 Technology TM Demonstrator,” *American Helicopter Society 67th Annual Forum, Virginia Beach, VA*, 2011.
- [5] Lorber, P., Law, G., O’Neill, J., Matalanis, C., and Bowles, P., “Overview of S-97 RAIDER Scale Model Tests,” *American Helicopter Society 72th Annual Forum, West Palm Beach, FL, USA, 17-19 May*, 2016.
- [6] Bowles, P., Matalanis, C., Wake, B., Berry, B., Bartz, E., and Scott, M., “A Model-Scale Wind-Tunnel Study of Main Rotor/Propeller Interference,” *American Helicopter Society 72th Annual Forum, West Palm Beach, FL, USA, 17-19 May*, 2016.
- [7] Stokkermans, T., Veldhuis, L., Soemarwoto, B., Fukari, R., and Eglin, P., “Breakdown of aerodynamic interactions for the lateral rotors on a compound helicopter,” *Aerospace Science and Technology*, Vol. 101, 2020, p. 105845. <https://doi.org/https://doi.org/10.1016/j.ast.2020.105845>.
- [8] Frey, F., Thiemeier, J., Öhrle, C., Keßler, M., and Krämer, E., “Aerodynamic Interactions on Airbus Helicopters’ Compound Helicopter RACER in Cruise Flight,” *Journal of the American Helicopter Society*, Vol. 65, No. 4, 2020, pp. 1–14. <https://doi.org/10.4050/JAHS.65.042001>.
- [9] Frey, F., Öhrle, C., Thiemeier, J., Keßler, M., and Krämer, E., “Aerodynamic Interactions on Airbus Helicopters’ Compound Helicopter RACER in Hover,” *Vertical Flight Society 76th Annual Forum*, 2020.
- [10] Öhrle, C., Schaferlein, U., Keßler, M., and Krämer, E., “Higher-order Simulations of a Compound Helicopter using Adaptive Mesh Refinement,” *the AHS International 74th Annual Forum & Technology Display, Phoenix, Arizona, USA*, 2018.
- [11] Öhrle, C., Frey, F., Thiemeier, J., Keßler, M., and Krämer, E., “Coupled and Trimmed Aerodynamic and Aeroacoustic Simulations for Airbus Helicopters’ Compound Helicopter RACER,” *Journal of the American Helicopter Society*, Vol. 64, 2019, pp. 1–14. <https://doi.org/10.4050/JAHS.64.032003>.
- [12] Thiemeier, J., Öhrle, C., Frey, F., Keßler, M., and Krämer, E., “Aerodynamics and flight mechanics analysis of Airbus Helicopters’ compound helicopter RACER in hover under crosswind conditions,” *CEAS Aeronautical Journal*, Vol. 11, No. 1, 2020, pp. 49–66. <https://doi.org/https://doi.org/10.1007/s13272-019-00392-3>.
- [13] Boisard, R., “Aerodynamic investigation of rotor/propeller interactions on a fast rotorcraft,” *44th European Rotorcraft Forum, Delft, The Netherland*, 2018.
- [14] Buehler, M., and Newman, S., “The aerodynamics of the compound helicopter configuration,” *The Aeronautical Journal*, Vol. 100, No. 994, 1996, pp. 111–120. <https://doi.org/doi:10.1017/S0001924000027391>.

- [15] Yeo, H., and Johnson, W., “Aeromechanics analysis of a compound helicopter,” Tech. rep., Army Research Development and Engineering Command, Moffett Field, CA Aviation, 2006.
- [16] Leishman, J. G., and Bi, N.-p., “Experimental investigation of rotor/lifting surface interactions,” *Journal of aircraft*, Vol. 31, No. 4, 1994, pp. 846–854. <https://doi.org/https://doi.org/10.2514/3.46570>.
- [17] Steijl, R., Barakos, G. N., and Badcock, K., “A framework for CFD analysis of helicopter rotors in hover and forward flight,” *International Journal for Numerical Methods in Fluids*, Vol. 51, No. 8, 2006, pp. 819–847. <https://doi.org/10.1002/flid.1086>.
- [18] Biava, M., Woodgate, M., and Barakos, G. N., “Fully implicit discrete-adjoint methods for rotorcraft applications,” *AIAA Journal*, Vol. 54, No. 2, 2015, pp. 735–749. <https://doi.org/https://doi.org/10.2514/1.J054006>.
- [19] Antoniadis, A., Drikakis, D., Zhong, B., Barakos, G., Steijl, R., Biava, M., Vigevano, L., Brocklehurst, A., Boelens, O., Dietz, M., et al., “Assessment of CFD methods against experimental flow measurements for helicopter flows,” *Aerospace Science and Technology*, Vol. 19, No. 1, 2012, pp. 86–100. <https://doi.org/10.1016/j.ast.2011.09.003>.
- [20] Steijl, R., and Barakos, G., “CFD analysis of complete helicopter configurations—lessons learnt from the GOAHEAD project,” *Aerospace Science and Technology*, Vol. 19, No. 1, 2012, pp. 58–71. <https://doi.org/https://doi.org/10.1016/j.ast.2011.01.007>.
- [21] Han, D., Pstrikakis, V., and Barakos, G. N., “Helicopter flight performance improvement by dynamic blade twist,” *Aerospace Science and Technology*, Vol. 58, 2016, pp. 445–452.
- [22] Garcia, A. J., and Barakos, G. N., “Numerical simulations on the ERICA tiltrotor,” *Aerospace Science and Technology*, Vol. 64, 2017, pp. 171–191. <https://doi.org/https://doi.org/10.1016/j.ast.2017.01.023>.
- [23] Jarkowski, M., Woodgate, M., Barakos, G., and Rokicki, J., “Towards consistent hybrid overset mesh methods for rotorcraft CFD,” *International Journal for Numerical Methods in Fluids*, Vol. 74, No. 8, 2014, pp. 543–576. <https://doi.org/10.1002/flid.3861>.
- [24] Zhang, T., and Barakos, G. N., “High-Fidelity CFD Validation and Assessment of Ducted Propellers for Aircraft Propulsion,” *Journal of the American Helicopter Society*, Vol. 66, No. 1, 2021, pp. 1–28. <https://doi.org/10.4050/JAHS.66.012008>.
- [25] Menter, F., “Two-Equation Eddy-Viscosity Turbulence Models for Engineering Applications,” *AIAA Journal*, Vol. 32, No. 8, 1993, pp. 1598–1605. <https://doi.org/https://doi.org/10.2514/3.12149>.
- [26] Rajagopalan, R. G., and Mathur, S. R., “Three dimensional analysis of a rotor in forward flight,” *Journal of the American Helicopter Society*, Vol. 38, No. 3, 1993, pp. 14–25. <https://doi.org/https://doi.org/10.4050/JAHS.38.14>.
- [27] O’Brien Jr, D. M., “Analysis of computational modeling techniques for complete rotorcraft configurations,” Ph.D. thesis, Georgia Institute of Technology, 2006.
- [28] Stokkermans, T., van Arnhem, N., Sinnige, T., and Veldhuis, L., “Validation and Comparison of RANS Propeller Modeling Methods for Tip-Mounted Applications,” *AIAA Journal*, Vol. 57, 2018, pp. 1–15. <https://doi.org/10.2514/1.J057398>.

- [29] Chaffin, M. S., and Berry, J. D., "Helicopter Fuselage Aerodynamics Under a Rotor by Navier-Stokes Simulation," *Journal of the American Helicopter Society*, Vol. 42, No. 3, 1997, pp. 235–243. <https://doi.org/https://doi.org/10.4050/JAHS.42.235>.
- [30] Barakos, G., Fitzgibbon, T., Kusyumov, A., Kusyumov, S., and Mikhailov, S., "CFD simulation of helicopter rotor flow based on unsteady actuator disk model," *Chinese Journal of Aeronautics*, Vol. 33, No. 9, 2020, pp. 2313–2328. <https://doi.org/https://doi.org/10.1016/j.cja.2020.03.021>.
- [31] Mavriplis, D. J., "Discrete adjoint-based approach for optimization problems on three-dimensional unstructured meshes," *AIAA journal*, Vol. 45, No. 4, 2007, pp. 741–750. <https://doi.org/https://doi.org/10.2514/1.22743>.
- [32] Biava, M., and Barakos, G. N., "Optimisation of ducted propellers for hybrid air vehicles using high-fidelity CFD," *The Aeronautical Journal*, Vol. 120, No. 1232, 2016, pp. 1632–1657. <https://doi.org/doi:10.1017/aer.2016.78>.
- [33] Zhang, T., and Barakos, G. N., "High-fidelity numerical analysis and optimisation of ducted propeller aerodynamics and acoustics," *Aerospace Science and Technology*, Vol. 113, 2021, p. 106708. <https://doi.org/https://doi.org/10.1016/j.ast.2021.106708>.
- [34] Sacks, J., Schiller, S. B., and Welch, W. J., "Designs for Computer Experiments," *Technometrics*, Vol. 31, No. 1, 1989, pp. 41–47. <https://doi.org/10.1080/00401706.1989.10488474>.
- [35] Bouhlel, M. A., Hwang, J. T., Bartoli, N., Lafage, R., Morlier, J., and Martins, J. R. R. A., "A Python surrogate modeling framework with derivatives," *Advances in Engineering Software*, 2019, p. 102662. <https://doi.org/https://doi.org/10.1016/j.advengsoft.2019.03.005>.
- [36] Kraft, D., "Algorithm 733: TOMP-Fortran Modules for Optimal Control Calculations," *ACM Transactions on Mathematical Software*, Vol. 20, No. 3, 1994, pp. 262–281. <https://doi.org/https://doi.org/10.1145/192115.192124>.
- [37] Johnson, S., "The NLOpt Nonlinear-Optimization Package," <https://nlopt.readthedocs.io/en/latest/>, retrieved 3 Sep 2020.
- [38] Jones, D. R., Schonlau, M., and Welch, W. J., "Efficient global optimization of expensive black-box functions," *Journal of Global optimization*, Vol. 13, No. 4, 1998, pp. 455–492. <https://doi.org/https://doi.org/10.1023/A:1008306431147>.
- [39] Blank, J., and Deb, K., "Pymoo: Multi-Objective Optimization in Python," *IEEE Access*, Vol. 8, 2020, pp. 89497–89509.
- [40] Grunwald, K. J., and Goodson, K. W., "Aerodynamic loads on an isolated shrouded-propeller configuration for angles of attack from -10 degrees to 110 degrees," Tech. rep., NASA-TN-D-995, 1962.
- [41] Zhang, T., Qiao, G., Smith, D., Barakos, G., and Kusyumov, A., "Parametric study of aerodynamic performance of equivalent ducted/un-ducted rotors," *Aerospace Science and Technology*, Vol. 117, 2021, p. 106984. <https://doi.org/https://doi.org/10.1016/j.ast.2021.106984>.
- [42] Sugawara, H., and Tanabe, Y., "Numerical Investigation of Rotor/Wing Aerodynamic Interactions at High Advance Ratios," *Journal of Aircraft*, Vol. 56, No. 6, 2019, pp. 2285–2298. <https://doi.org/10.2514/1.C035370>.